




# Graphene Aerogels: Structure Control, Thermal Characterization and Thermal Transport

Qin Wang<sup>1</sup> · Liping Xiang<sup>1</sup> · Di Mei<sup>1</sup> · Yangsu Xie<sup>1</sup> 

Received: 26 August 2020 / Accepted: 10 September 2020 / Published online: 22 September 2020  
© Springer Science+Business Media, LLC, part of Springer Nature 2020

## Abstract

Graphene aerogel (GA) as one of the innovative carbon nanostructured materials is superior with flexibility, strong mechanical strength, lightweight, high porosity and excellent durability, which attracted wide research interests and fulfill the requirements for various novel applications in energy conversion and storage, sensor, thermal management, and environment areas, etc. The thermal property among other important properties of GA is important for its novel applications. In this work, we first introduce the synthesis and microstructure control method for GA, including pore size control, anisotropic pore structure control, and heterostructure control. The methods for measuring the thermal conductivity of bulk GAs in air (apparent  $k$ ) and the  $k$  of solid matrix of GAs are introduced in detail, respectively. Finally, we review the thermal transport models for GAs, including the air–solid coupling models, models for calculating the intrinsic thermal properties of graphene nanoflakes, as well as the thermal reffusivity model and dominating thermal contact resistance model. Challenges and opportunities in the study of thermal transport in 3D GAs are discussed. Considering the remarkable complexity of physical/chemical structure of GAs, there is still a large room in understanding fundamentals of energy transport in these three-dimensional graphene networks, which will pave the way toward their novel applications in the near future.

**Keywords** Graphene aerogel · Micro-structure control · Thermal characterization · Thermal transport models

---

Qin Wang and Liping Xiang contributed equally to this work.

---

✉ Yangsu Xie  
ysxie@szu.edu.cn

<sup>1</sup> College of Chemistry and Environmental Engineering, Shenzhen University, Shenzhen 518055, Guangdong, People's Republic of China

## 1 Introduction

In recent years, stimulated by the increasing demands of novel applications, different innovative carbon nanostructured materials have been synthesized and extensively studied [1–3]. Three dimensional graphene aerogel (GA) is superior with flexible shape, strong mechanical strength, lightweight, high porosity and excellent durability. Extensive work has been done for the applications of GA in electrochemical devices [4, 5], pollution treatment [6–9], energy conversion [10], sensors [3], and energy storage [11], etc. The thermal property among other important properties of GA becomes increasingly important for their applications [12–17]. Thermal conductivity ( $k$ ) and diffusivity ( $\alpha$ ) of GA depend on their inner micro-structures, which includes the porosity, chemical doping, structural domain size, defects densities, and strength of interconnection among nanoparts, etc. For example, in the fields of super thermal insulation materials [12], thermoelectricity [13], solar water desalination [14], Joule-heating assisted water–oil separation [15], etc. By reducing the density, reducing the pore structure, or chemical doping of the GA,  $k$  of GA can be greatly lowered down. The ultra-low  $k$  significantly improved the overall energy utilization efficiency of the device and effectively reduced the weight of the system. On the other hand, in the fields of thermal management [16] and phase change materials [17] by improving the crystallinity and structural order, GA can be used as a fast heat transfer channel, thereby improving the heat dissipation performance of the composite materials. Therefore, it is of great significance to efficiently characterize the thermal properties of GA, study the heat transfer performance and mechanism, so as to promote its wide applications.

As a synthetic highly porous material, aerogel is derived from a gel by replacing the liquid inside it with air. Although graphene has a high intrinsic  $k$ , three-dimensional aerogels with graphene as the building elements have ultra-low  $k$  [18, 19]. Combined with its high porosity, strong mechanical elasticity and controllable functional groups at the surfaces, GA is expected to be an outstanding thermal insulating material. The development of thermal measurement technology facilitates the study on the thermal properties of carbon nanostructured materials. Laser reflectance (pump probe) technique [20], Raman technique [21, 22], microbridge method [23],  $3\omega$  technique [24], laser flash technique [25], and photothermal technique [26] have been used for thermal characterization of carbon materials. However, the unique structure of GA generates new challenges for effective macro-scale thermal characterization due to its rough surfaces, three-dimensional, self-assembling internal nanostructures, high porosity, and structural softness. For measuring the thermal conductivity of bulk GAs in air (apparent  $k$ ), hot disk method and the infrared microscopy technique have been used. To further avoid the significant measurement uncertainty resulted from the rough surfaces and the large thermal contact resistance due to the structural softness, the new differential laser heating and infrared imaging (DLI) technique is developed. For measuring  $k$  of the solid matrix of GAs, the transient electrothermal (TET) technique and steady-state electrothermal (SET) technique have been developed.

The heat transfer inside GAs is mainly from the coupling of the solid heat transfer, air heat transfer, and radiant heat transfer. In the analysis of the thermal conduction, the strong thermal radiation effect needs to be carefully subtracted. Considering the conduction of air, the size, shape and direction of the internal pores affect the heat transfer of GAs. When the size of the pores is less than a certain threshold,  $k$  of the air in the pores is inhibited (Knudsen effect), thereby greatly reducing  $k$  of GAs. The coupling relationship between solid and air thermal conduction and their contribution to effective  $k$  are related to the solid  $k$ , porosity, pore size and morphology. To study the heat transfer inside GAs, various models have been developed. Furthermore, from the perspective of solid heat conduction of the graphene matrix, phonons are the main heat carriers. Structural defects provide a large number of scattering opportunities for the propagation of phonons, thereby inhibiting the thermal conduction. However, the phonon scattering mechanism caused by the defects (density, type, chemical-doping) and crystal structure (crystal size, amorphous structure, grain boundary bonding, etc.) of GAs is very complicated, and it is difficult to be quantitatively measured. GAs are composed of self-assembled graphene or reduced graphene oxide nanoflakes, where the interconnection is through mainly Van der Waals interactions. When the bondings of the neighboring nano-flakes are weak, the strong thermal contact resistant among nano-flakes play a dominating role in the thermal transport process.

In this work, we review the studies about the synthesis, microstructure control, thermal characterization, and thermal transport models of GAs to uncover challenges, address technical issues in thermal characterization, and provide guidance on the applicability of current models in studying the coupled energy transport in the three dimensional GAs. In Sect. 2, we introduce the synthesis and microstructure controlling method for GAs, including the pore size control, anisotropic pore structure control, and heterostructure design. In Sect. 3, for measuring  $k$  of bulk GAs in air (apparent  $k$ ), hot disk method and the infrared microscopy technique, as well as the new differential laser heating and infrared imaging (DLI) technique will be introduced. In Sect. 4, for measuring  $k$  of the solid matrix of GAs, the transient electrothermal (TET) technique and the steady-state electrothermal (SET) technique will be introduced in detail. The method for subtracting the strong thermal radiation effect is further illustrated. In Sect. 5, the thermal transport models for GAs, including the air–solid coupling models, the models for the intrinsic thermal diffusivity/conductivity of GA from empirical formulas and heat transfer path method, the thermal reffusivity model for analyzing the effect of structure defects on phonon scattering, and the interface-mediated thermal conduction model in GAs with weakly interconnected structure will be illustrated and the relating works will be systematically reviewed.

## 2 Synthesis and Micro-structure Control

In order to meet the specific requirements of the novel applications, graphene aerogels are often designed to have different microstructures. Chemical doping (O, N, S, P, B and other single element doping and co-doping of two elements) [27–29],

density [30] and pore structure adjustment [31] are widely used in the design of GA. In this section, the synthesis and micro-structure control methods of GAs will be reviewed.

## 2.1 Synthesis Method

In 2000s, a three-dimensional (3D) carbon foam was first reported based on the nanostructure of graphite [32]. After that, with the deepening of research on graphene materials in recent years, the controllable preparation technology of 3D graphene materials has been rapidly developed. As a synthetic highly porous material, aerogel is derived from a gel by replacing the liquid inside it with air. The main preparation methods of GAs include the template method [33–35], self-assembly [36, 37], 3D printing method [38, 39] and so on. In recent years, 3D printing technology has been used to construct three-dimensional GAs [40, 41]. 3D printing is a rapid prototyping technology based on digital models, which constructs three-dimensional entities through layered processing and iterative forming [38, 39]. However, it is still difficult to use the 3D printing technology to adjust the pore diameters and morphology of GAs. Also the production process is complicated and expensive. Therefore, the most common methods for synthesizing GAs are self-assembly and ice template method, which are our focus in this work.

The ice template method is to use ice crystals formed during the freezing process as a template to prepare porous aerogels. Considering the hydrophobic nature of graphene, the hydrophilic graphene oxide (GO) is usually used as the precursor. To obtain a stable inter-connecting structure among GO nanoflakes during freeze casting, various binders could be used such as poly vinyl alcohol (PVA) [42, 43], cellulose [44, 45], ethanol [46], etc. After freeze drying or supercritical drying to replace the ice template by air, GAs can be prepared. In 2004, Wicklein et al. synthesized a novel three-dimensional foam structure with anisotropic pore structure through freeze casting. This three-dimensional structure had low  $k$ , strong mechanical hardness and flame retardant properties [45]. By controlling the freezing rate [47, 48] and direction [33, 46], GAs with difference pore size and pore morphology can be obtained.

The self-assembly method is a method by reducing GO nanoflakes in a solution. As the reduction process goes on, the hydrophilic GO nanoflakes become more and more hydrophobic, which induces a self-assembling process of the nanoflakes. Then GAs can be obtained by following freeze-drying or supercritical drying treatment [36, 37, 49]. The self-assembly method can be divided into in situ assembly and reduction assembly method. The in situ assembly means that when the graphene oxide solution reaches a certain concentration, these sheets can form a stable three-dimensional structure by overlapping with each other in the process [36, 37]. Xu et al. took the lead in synthesizing self-assembled graphene hydrogel by using a one-step hydrothermal method [36]. They found that when the concentration of the graphene solution reached  $1 \text{ mg}\cdot\text{ml}^{-1}$ , after hydrothermal treatment, the graphene nanosheets would be assembled in situ to form a continuous three-dimensional structure. The stability of GO in the solution was closely related to the pH of the solution. Bi

et al. [50] used acid and alkali to adjust the pH of the GO dispersion. As shown in the Fig. 1, when an appropriate amount of ammonia was added to the dispersion to adjust the pH of the dispersion system to about 10, the GO nanosheets formed a three-dimensional structure through self-assembling. Followed by freeze-drying and thermal annealing treatment, GAs with good elasticity were obtained.

The self-assembling process can also be promoted by the chemical reduction using reduction agents. In 2013, Gao et al. prepared an ultra-flyweight of GA by freeze-drying a solution of carbon nanotubes and large sheets of graphene. Its density was  $0.16 \text{ mg}\cdot\text{cm}^{-3}$ , which was lower than that of air ( $1.29 \text{ mg}\cdot\text{cm}^{-3}$  under standard conditions) [51]. This made GA the lowest density solid material known in the world. Hu et al. realized a highly elastic GA by using ethylenediamine as reduction agent and following freeze-drying [49]. The  $k$  of the resulting elastic GA was further studied by Xie et al. and was reported to be as low as  $0.2\text{--}0.4 \text{ mW}\cdot\text{m}^{-1}\cdot\text{K}^{-1}$  [19]. It was found that the aerogel pore structure could be designed by changing the shape of the reaction vessel and adding media. By adding other reducing agents or metal nanoparticles during the self-assembly process, the researchers could further tune the properties of the as-synthesized GA, including the electrical conductivity, mechanical flexibility, or hydrophobic properties, so as to meet various application requirements [52–54].

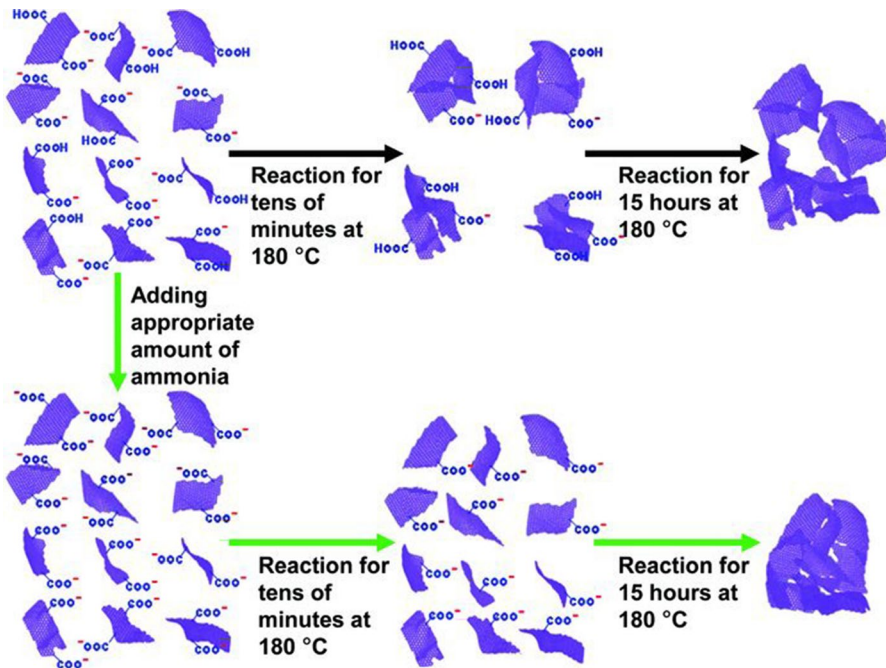


**Fig. 1** Process of GA formation with the addition of different quantities of ammonia [50]. By adding appropriate amount of ammonia to adjust the PH and followed by high temperature reaction, the self-assembling process can be facilitated. (Reproduced from Ref. [50] with permission from the Wiley–VCH)

## 2.2 Pores Size Control Methods

The size of the pores is one of the most critical factors determining the thermal properties of GAs. It is generally found that the smaller pores size leads to a lower  $k$  by reducing the effect of air thermal conduction. There are many factors influencing the pore size of the resulting GA, such as the concentration of GO [55], viscosity of the solution [56], freezing rate [45, 48], etc. The common method of controlling the pore size is to control the ice crystal formation by changing the freezing temperature and rate [57]. Pot et al. [48] used the directional freezing method to prepare adjustable pore size and morphology collagen scaffold with unidirectional pores by changing the freezing temperature during the freezing casting process. With the freezing temperature increasing, the number of ice crystal nucleation increased and the pore size decreased. Wicklein et al. [45] prepared CNF–GO–BA–SEP nanocomposite foam. The cooling rate of the mixture was controlled by changing the thermocouple and the electric heating element inserted into the copper rod. When the freezing speed was increased from 1 to 15 K·min<sup>-1</sup>, the pore size was found to be from ~100 to 20 μm.

In addition, the pore size can also be reduced by using supercritical drying technology [18, 58, 59]. The principle of supercritical drying technology is to adjust the temperature and pressure during drying process, so as to make the solvent in the gel reaches its own critical point, thus realizing the transition from liquid phase to gas. Supercritical drying does not damage the structure of the aerogel, thus it is able to maintain the original structure of the gel to the greatest extent. Yue et al. [18] prepared nitrogen-doped GAs using the CO<sub>2</sub> supercritical drying method. Their experiments showed that the pore size of GAs prepared by this method was much smaller than from freeze-drying, mostly in the order of tens of nanometers. It was worth noting that the lowest  $k$  of the prepared nitrogen-doped GAs was reported to be only 0.023 W·m<sup>-1</sup>·K<sup>-1</sup>, which was lower than that of static air and showed a good thermal insulation performance.

Furthermore, the size and morphology of pores can also be controlled by adding extra templates [30, 57, 60, 61] during freeze-casting. Peng et al. [30] used modified polystyrene (PS) spheres as sacrificial template to generate reduced graphene oxide/polyimide (r-GO/PI) nanocomposites with a hollow spherical pores structure (Fig. 2), which could further impedes heat transfer of air and leads to ultra-low  $k$  of 9 mW·m<sup>-1</sup>·K<sup>-1</sup>. Inspired by polar bear hair structure, Cui et al. [57] prepared a biomimetic carbon aerogel fiber with a hollow structure by freeze-casting and freeze-spinning technique. This biomimetic structure showed excellent heat insulation performance and a strong tensile strength. Zhan et al. [61] were also inspired by the same structure to prepare a carbon aerogel composed of fibers with a hollow structure. The carbon nanotubes were wrapped on the surface of Te through a hydrothermal process to form a hydrogel, which was then freeze-dried to form aerogel. After that, Te was removed by calcination to form a hollow structure. Since the pore size was smaller than the air free path, the air flow was greatly inhibited, resulting in an ultralow  $k$  (23 W m<sup>-1</sup>·K<sup>-1</sup>).

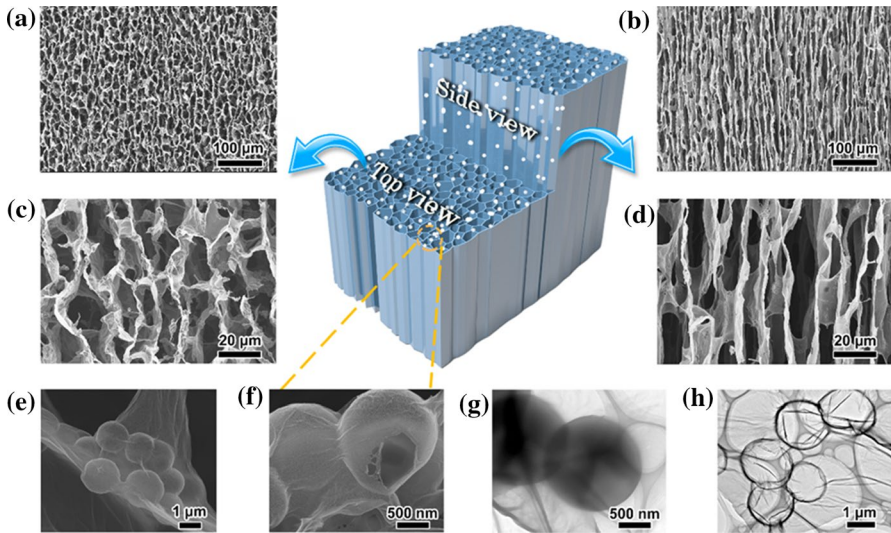


**Fig. 2** Microstructures of thermally insulating reduced graphene oxide/polyimide nanocomposite foams by adding PS micro-spheres as extra template [30]. (Reproduced from Ref. [30] with permission from the American Chemical Society)

### 2.3 Anisotropic Structure Design

For applications where the anisotropic thermal properties are required, the pore direction of GAs can be controlled. The common method to control the pore direction is by using the directional freezing casting method [33–35, 46, 59, 62–67], whose principle is to control the direction of ice crystal formation by building anisotropic temperature gradients. When the temperature of the cold substrate is below the freezing point of the suspension, the solvent first crystallizes and nucleates near the cold surface, and then grows along the direction of the temperature gradient to form ordered ice crystals. At the same time, the solute is repelled by the ice crystals, and then compressed between the ice crystals [67]. Subsequently, the ice crystals are removed by freeze-drying, resulting in a porous GA material with an ordered structure.

The oriented pores and wall structure lead to a strong anisotropic thermal behavior of GA. This is a consequence of a combination of orientation-dependent solid conduction in the walls and thermal radiation as well as possibly natural convection in the oriented direction. The apparent  $k$  in the oriented direction (along the pores) is expected to be significantly higher than in the other direction. Wicklein et al. [45] prepared CNF–GO–BA–SEP nanocomposite foam with anisotropic pore structure by using the freeze casting method. The  $k$  of this nanocomposite was  $170 \text{ mW}\cdot\text{m}^{-1}\cdot\text{K}^{-1}$  in the axial direction (along the pores) and  $15 \text{ mW}\cdot\text{m}^{-1}\cdot\text{K}^{-1}$  in the radial direction, respectively. In Peng et al. [30]’s work, for the reduced graphene oxide/polyimide (r-GO/PI) nanocomposites, the  $k$  in the radial direction reached as low as  $9 \text{ mW}\cdot\text{m}^{-1}\cdot\text{K}^{-1}$ , while in axial direction was

$58 \text{ mW}\cdot\text{m}^{-1}\cdot\text{K}^{-1}$ . Therefore, the oriented porous structure synthesized by freeze-casting method can be used for achieving highly anisotropic thermal performance. The anisotropic graphene porous structure has been widely used as thermal filler to develop graphene-polymer nanocomposite for the application of thermal interface materials in recent years [68–70]. The aligned and interconnected graphene/reduced graphene oxide chains provide thermally conductive pathway array throughout the composites for achieving high  $k$  along the alignment direction.

In addition to the unidirectional freezing, bidirectional [65, 66] and radial pores structure [33, 34] have also attracted wide attention. Researchers achieved a bidirectional freezing by using thermally insulating medium such as PDMS in the container to adjust the temperature gradient [65, 66]. For example, Bai et al. [65] controlled the inclination angle of the polydimethylsiloxane (PDMS) wedge and the cooling rate simultaneously, which generated two temperature gradients in both the vertical and horizontal direction. As is shown in the Fig. 3, the slurry froze starting from the bottom to the top of the wedge resulted from the temperature gradient, which made the ice crystals grew vertically and horizontally along the PDMS wedge. As a result, a porous structure with bidirectional pores was obtained. Additionally, Wang et al. [33] used the temperature difference between the container and the surroundings to achieve radial pore. After freezing, the ice crystals grew along radial direction. The channel size gradually decreased from the edge to the core position. The GA of mimetic turbine blades was obtained after freeze-drying. The aerogel with this structure exhibited excellent adsorption capacity in handling organic dyes besides super compressibility.

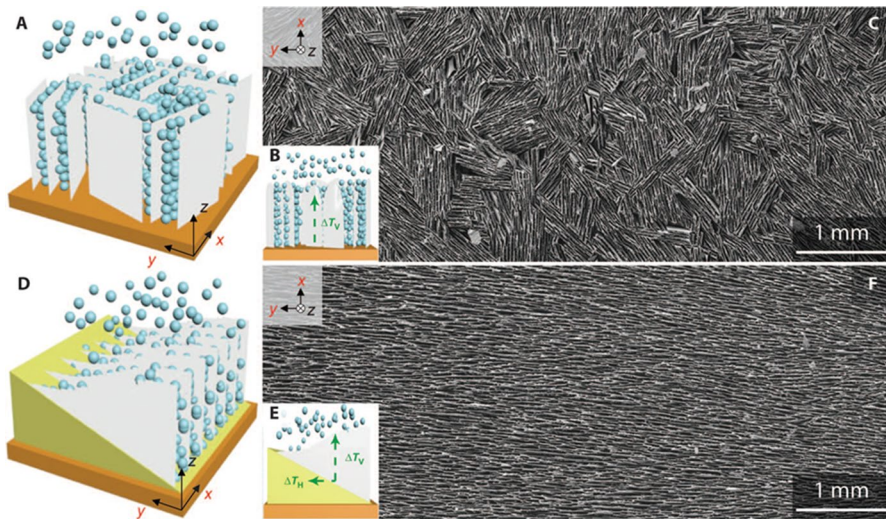


**Fig. 3** Schemes of unidirectional and bidirectional freeze-casting techniques which adjusted the ice growing directions as template for synthesizing anisotropic GAs [65]. (Reproduced from Ref. [65] by Bai et al. is licensed under CC BY)



## 2.4 Heterostructure Design

In order to meet the specific requirements of novel applications, GAs have been designed to have heterostructures. There are mainly two kinds of heterostructure design. One is chemical doping, and another is introducing new 1D or 2D structures. The chemical modification of graphene-based materials are mainly based on the active oxygen-containing groups on the surface of the material [39]. Common modification methods can be divided into non-metal doping [28, 71–73], metal doping [74–76], co-doping [77, 78] and so on. Non-metal doping include N-doping [71, 72, 79, 80], S-doping [28, 73] and co-doping with multiple elements [77, 78, 81, 82]. Deng et al. [72] prepared GAs with different nitrogen-doped structures by using EDA as nitrogen source and following thermal annealing at different temperatures (Fig. 4). The N-doped GA showed an apparent  $k$  of  $0.17\text{--}0.20\text{ W}\cdot\text{m}^{-1}\cdot\text{K}^{-1}$  in room temperature in air. Sulfur has similar electronegativity characteristics to carbon [28]. Chen et al. [28] prepared S-doped graphene foam by one-step solvent-thermal method, which used  $\text{Na}_2\text{S}$  as sulfur source. In their experiment,  $\text{Na}_2\text{S}$  was added to GO suspension in oil bath, which acted as a reducing agent for preparing S-doped graphene foam. The resultant S-doped graphene foam showed superior electrocatalytic activity and stability.

In addition, the heterostructures can also be achieved by introducing other 1D (such as carbon nanotubes [51, 83, 84], metals nano-wires [3, 85], etc.) or 2D materials (such

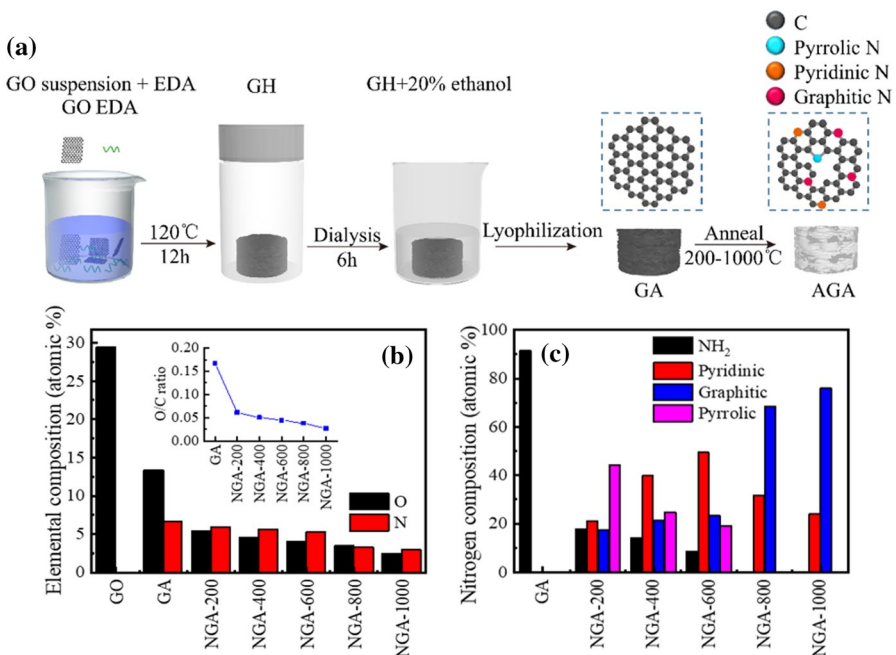


**Fig. 4** Schematic of the fabrication and structural characterization of N-doped GAs by using EDA as nitrogen source and following thermal annealing at different temperatures [72]. (Adapted from Ref. [72] with permission from the American Chemical Society)

as MoS<sub>2</sub> [75, 86], BN [68], etc.) into the structure of GAs. Since CNT and graphene have similar mechanical strength, good electrical and  $k$ , aerogels composed of CNTs and graphene have been widely studied [51]. Gao et al. prepared ultra-flyweight aerogels (UFAs) by freeze-drying the mixture of CNT and GO, which had ultralow density ( $\rho \geq 0.16 \text{ mg}\cdot\text{cm}^{-3}$ ) and high porosity (99.9%) [51]. Given their unique structure, UFAs showed an ultrahigh absorption capacity of oil and organic liquids. MoS<sub>2</sub> is a typical transition metal sulfide, which structure is like graphene. It consists of 3 atoms (S-Mo-S) stacked together through van der Waals interaction [87]. Feng et al. [74] prepared graphene hybrid beads with onion-like structure by combining the r-GO and MoS<sub>2</sub>, which achieved 74% evaporation efficiency under the illumination of power density of only  $0.5 \text{ kW}\cdot\text{m}^{-2}$ . Hu et al. [75] used GA as a support to prepare MoS<sub>2</sub>/GA. The prepared GA was immersed in solution of ammonium thiomolybdate (ATM), freeze-dried and annealed at  $450 \text{ }^\circ\text{C}$  under 2%H<sub>2</sub>/Ar to preparing MoS<sub>2</sub>/graphene hybrid aerogel. This composite structure combined the high specific surface area, high electrical conductivity, and  $k$  of GA, as well as the high sensitivity and selectivity for N<sub>2</sub>, CO and H<sub>2</sub>.

### 3 Characterization of the Apparent Thermal Conductivity

To study the thermal performance of GAs, it is of great significance to characterize the thermal properties of GA accurately. The apparent  $k$  is the thermal conductivity of bulk GAs in air, which includes the effect of solid conduction, air conduction, and thermal radiation. In the following section, the infrared imaging method and hot disk technique is reviewed in detail. A new technique named differential laser heating and infrared imaging (DLI) technique is also introduced for measuring the bulk  $k$  of GAs in air.

#### 3.1 Hot Disk Method

The hot disk transient plane source (TPS) method has been widely used for measuring  $k$  and  $\alpha$  of solid materials [88–90]. Briefly, when measuring  $k$  of aerogel, the probe is sandwiched between two identical samples. Then a constant current is applied to the probe to induce a constant joule heating power. As the temperature is increased, the resistance of the probe will be changed correspondingly. During the whole test, the voltage drop generated at both ends of the probe is recorded. Since the temperature of the probe is proportional to the voltage, the evolution of temperature with time can be built, so as to calculate  $k$  of the sample. The following assumptions are made: the probe thickness and heat capacity can be neglected; the probe is heated evenly and the power remains stable; compared with the probe, the sample is uniform and infinite;  $k$  of the sample is constant during the test. As a result,  $k$  of the sample can be expressed by the following formulas:

$$\Delta\bar{v}(\tau) = \frac{P_0}{(\pi^{3/2}ak)}D(\tau) \quad (1)$$

$$D(\tau) = \frac{1}{m^2(m+1)^2} \int_0^\tau \frac{d\sigma}{\sigma^2} \sum_{n=1}^m n \cdot \sum_{l=1}^m l e^{-\left(\frac{n^2+l^2}{m^2}\right)/4\sigma^2} \cdot I_0 \cdot \left(\frac{nl}{2m^2\sigma^2}\right) \quad (2)$$

Among them,  $\Delta\bar{v}(\tau)$  is the average temperature rise of the probe surface,  $a$  is the radius of the outermost heat ring of the annular heat source group;  $\tau$  is the dimensionless characteristic time  $\tau = \sqrt{\alpha t}/a$ ,  $t$  is the measuring time,  $\alpha$  is the thermal diffusivity of the material to be measured;  $\sigma$  is the integral variable and  $\sigma^2 = \alpha(t-t')/a^2$ ,  $m$  is the number of heat source rings;  $P_0$  is the heating power of the probe,  $I_0$  is the first kind of zero-order modified Bessel function. Then  $k$  of the sample can be calculated by the slope  $P_0/(\pi^{3/2}ak)$  [88].

Yue et al. prepared a batch of nitrogen-doped aerogel samples with different GO contents, and measured  $k$  of the samples by using the hot disk method. The measured  $k$  is in the range of 0.023–0.026 W·m<sup>-1</sup>·K<sup>-1</sup> at room temperature and under standard atmospheric pressure [18]. The hot disk method is a commercialized technique which is easy to use. However, due to the rough, soft, and porous structure of GA, the contact method resulted in significant contact thermal resistance, which brings in large measurement uncertainties. Thus, the non-contact thermal characterization methods based on infrared imaging have been developed.

### 3.2 Infrared Microscopy Technique

Infrared microscopy technique as a non-contact thermal characterization method is used for measuring the apparent  $k$  of the bulk materials. The experimental set-up is shown in Fig. 5a. During the measurement, the sample is sandwiched between two glass wafers. An appropriate amount of silver paste is applied between the sample and the glass wafers, which can reduce the thermal contact resistance to a great extent. Then they are placed between a heat sink and a heater of constant temperature. Assuming one dimensional heat transfer model, based on the Fourier's law, the heat flux passing through the cross section of the sample is equal to that of the reference glass wafers. Thus, the energy balance equation can be expressed as:

$$q = -k_{Glass} \cdot (dT/dx)_{Glass} = -k_{Sample} \cdot (dT/dx)_{Sample} \quad (3)$$

where  $q$  is the heat flux;  $k_{Glass}$  is the thermal conductivity of glass wafers,  $k_{Sample}$  is the thermal conductivity of sample;  $(dT/dx)_{Glass}$  and  $(dT/dx)_{Sample}$  are the temperature gradient of glass wafers and sample, respectively. Thus, the apparent  $k$  of the to-be-measured sample can be calculated according to the following formula:

$$k_{Sample} = \frac{k_{Glass} \cdot (dT/dx)_{Glass}}{(dT/dx)_{Sample}} \quad (4)$$

As the temperature reaches quasi-steady state, the temperature distribution of the side surface of the sample and the glass wafers are collected by using an infrared camera. To reduce the measurement errors from the unknown surface emissivity of the sample and the glass wafers, the side surface should be precoated with a thin

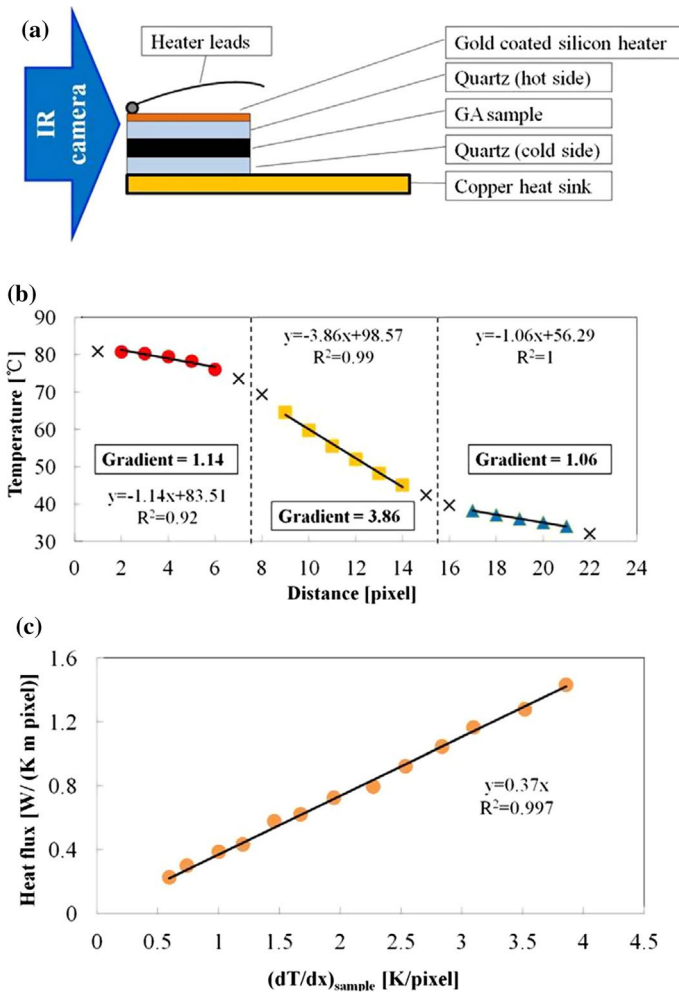


**Fig. 5** (a) Schematic of the thermal conductivity measurement set-up using the infrared microscopy technique. (b) Temperature curve of the glass and sample. (c) The relationship between the heat flux and temperature gradient. (Adapted from Ref. [29] with permission from Elsevier)

layer of graphite or black paint whose emissivity is known to reduce the error from the temperature measurement.

Fan et al. measured the  $k$  of GAs using infrared microscopy technique and investigated the effect of graphene volume fractions and thermal annealing on  $k$ . Figure 5 (b) shows a typical temperature and linear fitting curves of the glass and sample in their measurement. The  $k$  of the glass wafers used was  $1.3 \text{ W} \cdot \text{m}^{-1} \cdot \text{K}^{-1}$ . After obtaining an average gradient of two glass wafers layers, the rate between the gradient of sample and glass can be used to calculate  $k$  of sample based on Eq. 4. To improve the reliability, the relationship between the heat flux ( $q$ ) and temperature gradient ( $dT/dx$ ) in the sample area at different heating powers was further measured. As

is shown in Fig. 5c, the temperature distribution diagram of the sandwich structure were obtained under different heat flux. The temperature gradient was extracted from the least squares slope that was most suitable for the curve [29]. After the relationship between heat flux and ( $q$ ) and temperature gradient ( $dT/dx$ ) in the sample area was obtained,  $k$  of the sample was calculated based on Eq. 3 [91]. In Fan’s work, the gradient of hot and cold glass wafers were 1.14 and 1.06, respectively, while the gradient of sample was 3.86. The  $k$  of this GA sample was then determined to be  $0.36 \pm 0.015 \text{ W}\cdot\text{m}^{-1}\cdot\text{K}^{-1}$ . Ghasemi et al. also characterized  $k$  of a double-layer structure (DLS) composed of carbon foam layer and exfoliated graphene layer using the infrared microscopy method [91]. The corresponding  $k$  for the double-layered carbon structure was determined to be 0.309 and  $0.117 \text{ W}\cdot\text{m}^{-1}\cdot\text{K}^{-1}$  for exfoliated graphene layer and carbon foam layer, respectively. The  $k$  of these two layers was increased to 0.959 and  $0.426 \text{ W}\cdot\text{m}^{-1}\cdot\text{K}^{-1}$ , respectively, when this double-layer structure was filled with water.

### 3.3 Differential Laser Heating and Infrared Imaging (DLI) Technique

Although the infrared microscopy technique is a non-contact method, it still requires an accurate temperature scanning of the highly porous GA surface [29]. Likewise, laser flash technique has also been used to measure the apparent  $\alpha$  of carbon foams at room temperature [92]. However, considering the highly rough and porous surface of GA, there is also a certain error in directly using infrared scanning method to measure the temperature distribution of the surface of GA. Therefore, it can be further improved to adapt to the unique structure of GA.

The DLI technique is a new method for characterizing the apparent  $k$  of GAs by measuring the difference of the thermal resistance between the test and reference group. The experimental set-up is shown in Fig. 6a. The figure on the left is the reference group, where two glass wafers are stacked together on an aluminum

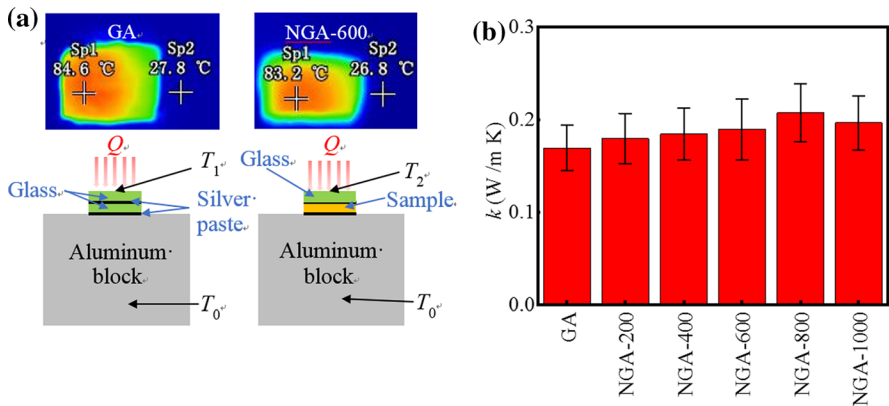


**Fig. 6** (a) Schematic diagram of the experimental setup for measuring  $k$  using the DLI method. The upper insets show the steady-state IR images of GA and NGA-600. (b) Measurement result of GA and NGAs. (Adapted from Ref. [72] with permission from the American Chemical Society)

block (heat sink). An appropriate amount of silver paste is applied between the interfaces to reduce the effect of thermal contact resistance. The surface of the upper glass wafer is coated with black paint (emissivity = 0.97) before the experiment. The right figure shows the test group, where the bottom glass wafer in the reference group is replaced by the to-be-measured sample. During the measurement, a laser of uniform power density is used to irradiate the upper surface of the glass wafer as heating source where the laser spot completely covers the sandwiched structure. The incident laser power is denoted as  $Q$ . An infrared camera is used to record the temperature of the upper surface. When the temperature collected by the infrared camera no longer changes (reaching quasi-steady state), the corresponding surface temperature is recorded as  $T_1$  for the reference group and  $T_2$  for the test group, respectively. During both experiments, the power density of the laser is controlled to be equal as  $Q$ . Since the upper surface of the glass wafers are coated with the same black paint, the laser absorption coefficient of the two groups can be regarded as equal, which makes sure that the absorbed laser power is the same for both groups.

Assuming one-dimensional thermal conduction model, according to the Fourier law, for the reference group:  $R_{Glass} + R_{Glass} = (T_1 - T_0)/Q$ ; while for test group:  $R_{Glass} + R_{Sample} = (T_2 - T_0)/Q$ , where  $R_{Glass}$  and  $R_{Sample}$  are thermal resistance of the glass wafers and sample, respectively;  $T_0$  is the temperature of the aluminum block, which stays constant during the measurement. Since the heat flux passing through the sandwiched structure of the two experiments can be assumed equal, the above heat transfer equations can be combined as:

$$\frac{T_1 - T_0}{2R_{Glass}} = \frac{T_2 - T_0}{R_{Glass} + R_{Sample}} \quad (5)$$

By measuring the temperature of the aluminum block  $T_0$ , the quasi-steady-state temperatures  $T_1$  and  $T_2$  of the upper glass of the reference group and the test group, respectively,  $R_{sample}$  can be calculated by the following formula:

$$R_{Sample} = \frac{2T_2 - T_0 - T_1}{T_1 - T_0} R_{Glass} \quad (6)$$

Since  $R$  is related to the thickness ( $d$ ) and  $k$  as  $R = d/k$ , the corresponding  $k$  value of the to-be measured sample can be determined subsequently.

Deng et al. used ethylenediamine as a nitrogen source and hydrothermal reduction to synthesizing N-doped GAs. By subsequent thermal annealing at different temperatures from 200 to 1000 °C in Ar atmosphere, GAs with different forms of nitrogen doping structure were obtained.  $k$  of these GA samples were measured by using the DLI technique. The insets in Fig. 6a shows the recorded infrared image of the top glass wafers surface for measuring GA and NGA-600 at quasi-steady state. Figure 6b shows the result of  $k$ . In Deng et al.' work,  $k$  of glass was  $0.723 \text{ W}\cdot\text{m}^{-1}\cdot\text{K}^{-1}$ .  $k$  of the group of samples was determined to be in the range of  $0.17\text{--}0.21 \text{ W}\cdot\text{m}^{-1}\cdot\text{K}^{-1}$ , indicating that thermal annealing did not significantly affect the apparent  $k$  of GA when the pores size was in the range of dozens of micrometers [72].

## 4 Thermal Characterization of Solid Matrix

When the pore size is smaller or comparable to the mean free path ( $\lambda$ ) of air molecules ( $\sim 70$  nm), the heat conduction of air within GA is sufficiently suppressed according to the Knudsen effect. Under this circumstance, the solid heat conduction of the graphene matrix plays a dominating role in the thermal transport of GA. Two-dimensional graphene nano-sheets are the basic unit of solids that constitute the three-dimensional GA, which are electrically conductive. In order to investigate the solid  $k$  of GA, and to more intuitively study the mechanism of internal phonon energy transport, the self-heating and self-sensing electrothermal technologies have been developed. Herein, the TET and SET technique for characterizing the solid thermal properties, including the effective  $\alpha$ ,  $k$  and  $c_p$  of GAs will be illustrated in Sects. 4.1 and 4.2, respectively. Then the method for subtracting the strong thermal radiation effect will be introduced in Sect. 4.3.

### 4.1 Transient Electro-Thermal (TET) Technique for Effective $\alpha$

The transient electrothermal (TET) technology is a cutting-edge thermal measurement technology with a wide range of applications. It has been applied to the measurement of  $\alpha$  of conductors, semiconductors and insulators, including carbon nanomaterials [93], GF [94], metal wires [95], polymer fibers [96], biological DNA fibers [97], etc. If the to-be-measured fiber/film is nonconductive, a thin film of metal should be coated on the upper surface of the sample to making it electrically conductive [95, 98]. GAs is electrical conductive [49], which means the coating is not required. In addition, GA has stable structure but porous and rough surface [72]. Thus, compared with other technologies (thermal plane source method [99],  $3\omega$  method [100], micro bridge method [101], etc.) which require either contact, metal coating, or direct infrared scanning, the TET technique has the following advantages in measuring the thermal properties of GAs: easy to operate, fast, no additional coating treatment required; low requirements on the surface temperature scanning.

Figure 7a shows the schematic of the experimental set-up of TET technique [102]. First, the to-be-measured samples were cut into rectangular films, then suspended between two silicon or copper or aluminium electrodes. For the soft GA, the ends of sample are compressed tightly with another two silicon wafers or metal clamps for the purpose of good contact between the sample and the electrode. The electrodes are connected to a current source and an oscilloscope in parallel. Then the whole device is built in a vacuum chamber where the air pressure is maintained below 0.5 mTorr. At the beginning of the experiment, a step current is applied to the sample by the current source, causing a transient Joule heating. Upon heating, the temperature of the sample has a fast increase and then reaches quasi-steady state through heat conduction to the electrode and heat radiation to the environment. Since the entire measurement process is carried out in a vacuum environment, the heat convection by air can be neglected. Within the small temperature range, the temperature coefficient of resistance of the sample is assumed to be constant.

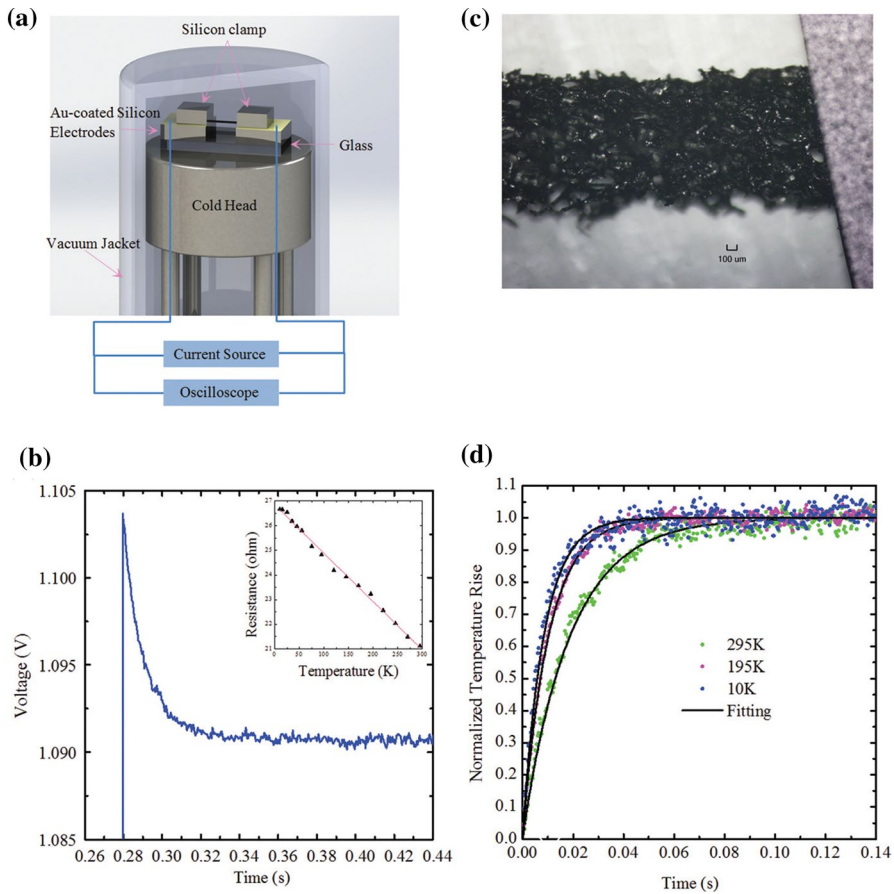


**Fig. 7** (a) The schematic for the TET technique. (b) The  $V-t$  curves measured at the temperatures of 195 K. The inset shows the linear fitting of the resistance change against temperature for GF sample 1 from 295 K to 10 K. (c) Microscopy image of sample 1 suspended between two silicon electrodes. (d) The normalized  $V-t$  curves of GF samples measured at different environmental temperatures (295 K, 95 K and 10 K) [103]. (Reproduced from Ref. [103], with the permission of RSC Publishing)

Hence, the normalized temperature change curve of sample can be obtained by normalizing the  $V-t$  curve collected by the oscilloscope. The normalized temperature  $T^*$  ( $T^* = [T(t) - T_0]/[T_\infty - T_0]$ ) can be obtained by integral of Green’s function as: [19]

$$T^* = \frac{48}{\pi^4} \sum_{m=1}^{\infty} \frac{(-1)^m}{m^2} \frac{1 - \exp[-m^2 \pi^2 \alpha_m t / L^2]}{m^2} \tag{7}$$

where  $m$  is the normalized parameter,  $\alpha_m$  is the thermal diffusivity of sample,  $t$  is time, and  $L$  is the length of the GA sample. From the equation, under the same conditions, a larger  $\alpha$  leads to a shorter time to reach steady state temperature. Based on



the experimental data, different methods can be used to obtain  $\alpha$  of the GA sample, including the linear fitting at the initial state of Joule heating, characteristic point method, and least square fitting method by using Matlab programming [95].

Xie et al. used the TET technique to characterize  $\alpha$  of GF [103]. Figure 7b shows the raw experimental data of the transient voltage change recorded by the oscilloscope. The inset reflects the linear fitting of electric resistance with temperature (from 295 K to 10 K). The microscopy image of the measured sample is shown in Fig. 7c, where the GF sample was suspended between two silicon electrodes. The corresponding normalized  $V$ - $T$  curve of the sample collected at different environmental temperatures are presented in Fig. 7d. The normalized  $V$  of the GF sample followed a quick increasing behavior to the quasi-steady state upon the joule heating. Additionally, it was found that when the environmental temperature went down from 295 K to 10 K, the time for the normalized  $V$  to reach quasi-steady state became shorter and shorter, which reflected that the  $\alpha$  of the sample was increased as the environmental temperature went down.

#### 4.2 Steady-State Electro-Thermal (SET) Technique for Effective $k$ and $c_p$

To characterize the effective  $k$  of GAs, the SET technique can be used [94]. The  $V$ - $t$  curve resulted from the TET joule heating includes both transient and steady-state phases, as is shown in Fig. 7b. While the TET technique extracts  $\alpha$  from the transient state, the SET technique determines  $k$  based on the quasi-steady state. Therefore, the experimental set up of the SET and TET technique are built in the same way [104]. When the temperature of the sample reaches quasi-steady state, a one-dimensional energy balance equation can be expressed as: [105]

$$k \frac{\partial^2 T(x)}{\partial x^2} + q_0 = 0 \quad (8)$$

In which  $q_0$  is the electrical heating power per unit volume, here  $q_0 = I^2 R_1 / A_C L$  is assumed to be a constant,  $I$  is the constant DC current applied to the sample,  $R_1$  is electrical resistance when the temperature of sample becomes stable,  $A_C$  and  $L$  are the cross-sectional area and suspended length of the sample, respectively.  $T(x)$  is the temperature at  $x$  position along the length of the sample. By solving the above equation, we can obtain the temperature distribution equation as [19]  $T(x) = -q(x^2 - L_x)/2k + T_0$ . Then the average temperature rise  $\Delta T = I^2 R_1 L / 12k A_C$  can be obtained by integral of  $T(x)$  with the sample length  $L$ . Within a small temperature range, the relationship between the temperature rise and the electrical resistance can be written as:  $\Delta T = \Delta R / (dR/dT)$ , where  $\Delta R$  is the electrical resistance change before and after the joule heating, and  $dR/dT$  is the first derivative of electrical resistance against temperature. Thus, the effective  $k$  of sample at quasi-steady state can be calculated as below [19]:

$$k_m = \frac{I^2 R_1 L}{12 A_C \Delta R} \cdot \frac{dR}{dT} \quad (9)$$

On the other hand, the relationship between  $k$  and  $\alpha$  can be expressed as: [19]  $k = \alpha \cdot \rho c_p$ , in which  $\rho$  and  $c_p$  are the density and heat capacity of the sample, respectively. Therefore, once  $k$  and  $\alpha$  are obtained,  $c_p$  of the sample at different temperatures can be calculated by this equation.  $c_p$  contains significant information about the structure of the materials [19]. The porous structure of GA is made up of r-GO sheets [106]. However, there is hardly any measurement about the  $c_p$  of r-GO. When it comes to the  $c_p$  of GO, it is usually taken equal to the value of graphite or amorphous carbon (AC) [19]. The combination of TET and SET technique provides an effective way for characterizing the  $c_p$  of carbon materials.

Xie et al. characterized the effective  $k$  of GA by using the SET technique [19]. In the experimental set-up, the GA sample was suspended between two silicon electrodes. The  $(dR/dT) - T$  curve is presented in Fig. 8a. It can be seen that  $dR/dT$  of the five GA samples followed a quick increasing behavior as the temperature went down. Then  $k$  was calculated by using the  $dR/dT$  data based on Eq. 9. The result for the measured  $k$  of the five GA samples is plotted in Fig. 8b, where the measured  $k$  of GA sample decreased with decreasing temperature.  $c_p$  of GA was further determined from the measured  $k$  and  $\alpha$  result as  $c_p = k_e / (\rho \alpha_e)$ , where  $k_e$  and  $\alpha_e$  are the measured effective  $k$  from the SET experiment and effective  $\alpha$  from the TET experiment, respectively.  $\rho$  was determined by measuring the mass and the volume of GA. Figure 8c shows the average  $c_p$  of the two groups of GAs in comparison with that of high-purity Acheson graphite [34], diamond-like carbon films and amorphous carbon (AC) [35]. As temperature went down from RT to 45 K,  $c_p$  of GA decreased linearly, where the trends and slopes were similar to that of graphite [36].

### 4.3 Thermal Radiation Effect

GA has very large specific surface area due to its high porosity, meaning that the thermal radiation effect could be so significant that it cannot be neglected. Hence, it is necessary to subtract the effect of thermal radiation from the measurement results for the purpose of reliable experimental results [103]. The  $\alpha_{\text{measure}}$  from the TET experiment is a combined effect of the real  $\alpha$  ( $\alpha_{\text{real}}$ ) and the radiation effect  $\alpha_{\text{measure}} = \alpha_{\text{real}} + \alpha_{\text{radiation}}$ , which was derived as: [19]

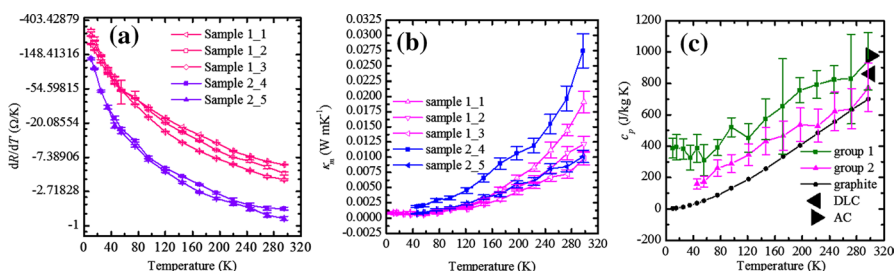


**Fig. 8** (a) The  $(dR/dT) - T$  curve of GA samples characterized by Xie et al. (b) The effective  $k$  of the five GA samples against temperature (c) The comparison of the average  $c_p$  for the GAs samples, high-purity Acheson graphite, diamond-like carbon films and AC. (Reproduced from Ref. [19], with the permission of the Elsevier)

$$\alpha_{measure} = \alpha_{real} + \frac{1}{\rho C_p} \cdot \frac{8\epsilon_r \sigma T^3}{D} \cdot \frac{L^2}{\pi^2} \tag{10}$$

In this equation, the first term is the real  $\alpha$  of GA, and the second term is from the thermal radiation effect.  $\epsilon_r$ ,  $D$ , and  $T$  are the emissivity, cross-sectional area, and the averaged temperature of the sample, respectively.  $\epsilon_r$  of GA can be assumed as equal to 1. From Eq. 10,  $\alpha_{measure}$  is linearly related to  $L^2$ . Therefore, the thermal radiation effect can be subtracted by linearly extrapolating the curve of  $\alpha_{measure}-L^2$  to the point of  $L^2 = 0$ . The intercept corresponds to  $\alpha_{real}$ .

Xie et al. studied the thermal radiation effect in GF by measuring the GF samples at different lengths. Figure 9 shows the comparison of the effective  $\alpha$  against temperature curve for the sample with different suspended lengths and width ( $L_1=5.14$  mm,  $L_2=3.74$  mm, and  $L_3=1.01$  mm). Obviously, under the same experimental conditions, the longer suspended length resulted in an larger effective  $\alpha$ . Then the  $\alpha_{real}$  which had no radiation effect was determined by linearly extrapolating the curve of effective  $\alpha-L^2$  to the point of  $L^2=0$  for the three GF samples, respectively. The inset shows the effective  $\alpha$  against length square ( $L^2$ ) for the three GF samples at temperature of 54 K, to show one of the fitting processes for determining  $\alpha_{real}$  of the sample. It was found that the thermal radiation had a very strong effect in the overall effective  $\alpha$  when the sample length was long.

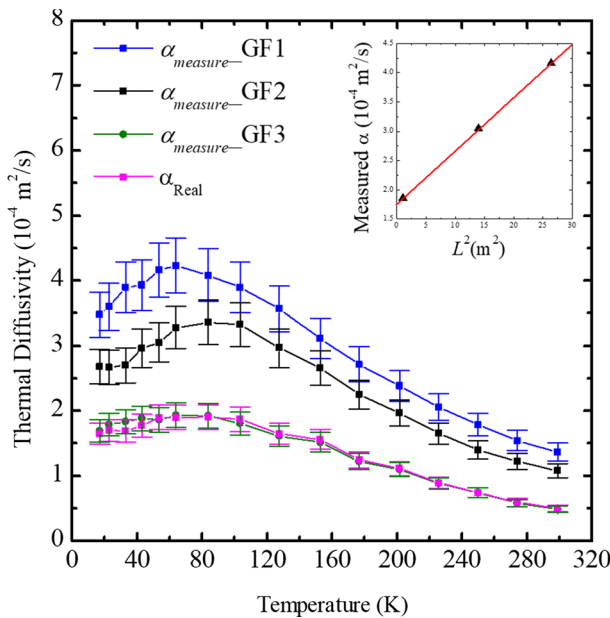


**Fig. 9** The  $\alpha_{measure}$  against temperature  $T$  for the three GF samples and the resulting real thermal diffusivity of GF ( $\alpha_{real}$ ). The inset shows the effective  $\alpha$  against length square ( $L^2$ ) for the three GF samples at temperature of 54 K. (Reproduced from Ref. [103], with the permission of RSC Publishing)

## 5 Thermal Transport Models

### 5.1 Air–Solid Coupling

The pore structure has a great influence on the apparent  $k$  of the three-dimensional graphene-based materials since the air conduction inside the pores could play a significant role when the pore size is not sufficiently reduced. As a result, the air–solid coupling heat conduction has attracted wide research attentions. Sakai et al. studied the variation of  $\alpha$  of highly porous materials with the pore size [107]. Wicklein et al. found that when the pore size changed from 150  $\mu\text{m}$  to 20  $\mu\text{m}$ ,  $k$  of porous graphene material did not change significantly [45]. Zhao et al. systematically studied the liquid–solid two-phase heat transfer model for the open pore structure of metal foams [108]. The models for computing  $k$  of two-phase materials based on  $k$  of the two phases and their volume fraction have been systematically compared in Wang et al.'s work [109]. These works paved the way for understanding the gas–solid coupled heat transfer in the three-dimensional structure of GAs.

Among the models, the rule of mixtures [110] have been applied to predict the range of  $k$  of the r GO nanosheets:

$$k_{GA} = fk_G + (1 - f)k_{air} \quad (11)$$

where  $f$  is the volume fraction of solid,  $k_G$  is the intrinsic  $k$  of the graphene nanosheets, and  $k_{air}$  is  $k$  of the air within pores. This model neglects the interconnection among the graphene nanosheets and consider GA as a simple mixture of graphene nano-sheets and air. It provides an estimate of  $k$  of the graphene portion of the aerogel.

The well-known Maxwell's effective medium approach has also been used for calculating the effective  $k$  of the graphene nanosheet network: [111]

$$k_{GA} = k_G \left[ \frac{3k_{air} + 2f(k_G - k_{air})}{(3 - f)k_G + k_{air}f} \right] \quad (12)$$

Bernal et al. used the Maxwell effective media model to calculate  $k$  of graphene matrix in reduced graphene oxide paper [111]. The in plane  $k$  values of the dense nanoflakes networks were calculated according to this model, which were 95  $\text{W}\cdot\text{m}^{-1}\cdot\text{K}^{-1}$  for the RGO nanopaper and 390  $\text{W}\cdot\text{m}^{-1}\cdot\text{K}^{-1}$  for the RGO-1700 at 25  $^\circ\text{C}$  [111]. To take the thermal contact resistance between the graphene nanosheets and air into consideration, a more detailed effective medium theory (EMT) [112] has also been used by Shahil et al. for estimating the intrinsic  $k$  of the graphene nanosheets:

$$k_{GA} = k_G \left[ \frac{3k_{air} + 2f(k_G - k_{air})}{(3 - f)k_G + k_{air}f + \frac{R_B k_{air} k_G f}{H}} \right] \quad (13)$$

where  $R_B$  is the thermal contact resistance between the graphene nanosheets and air, and  $H$  is the thickness of the nanosheets. The graphene sheet-liquid octane interface

thermal resistance was reported to be  $3.7 \times 10^{-9} \text{ K}\cdot\text{m}^2\cdot\text{W}^{-1}$  based on molecular dynamics simulations [113]. Fan et al. used a mixed model and an effective medium model to predict and analyze  $k$  of the two-phase system inside GA. They reported that  $k$  of chemically-derived graphene in their work is in the range of 12.2–30.2  $\text{W}\cdot\text{m}^{-1}\cdot\text{K}^{-1}$  [29].

It should be noted that these models still do not include the effect of interconnections among the graphene nano-sheets. In general, the Maxwell model is expected to be valid at low volume fractions ( $\varphi \ll 1$ , in the order of 0). Also it is assumed that the domains are spatially separated where the interactions among domains are insignificant [114]. However, the graphene nano-flakes inside GAs are interconnected with neighboring nanoflakes through the Van der Waals force and the  $\pi$ - $\pi$  interactions. Thus, the solid network within GAs is not like randomly distributed particles as that described in the Maxwell model [52], which makes the interface heat transfer between the solids cannot be neglected.

Recently, Zhao et al. [115] took both the inter-fiber thermal contact resistance and the intrinsic thermal resistance of nanofibers into consideration in their analytical model to predict  $k$  of nanofiber networks as a function of geometric and thermal properties. By using the statistical theory and Fourier's law of heat conduction, the model was derived as:

$$\frac{k_a}{k_0} = n_s A_0 \frac{Bi \langle N_c \rangle}{2 \langle |\cos \theta| \rangle L / \langle H \rangle + Bi \langle N_c \rangle} \langle |\cos \theta| \rangle \quad (14)$$

where  $k_a$  and  $k_0$  are the apparent thermal conductivity of the 3D networks and the intrinsic thermal conductivity of the nanofibers, respectively;  $L$  is the length of the nanofibers;  $A_0$  is the cross-sectional area of a single nanofiber;  $V_f$  is the volume fraction occupied by the nanofibers;  $\theta$  is the polar angles and  $\langle |\cos \theta| \rangle$  was derived to be  $2/\pi$  for 3D random networks;  $B_i = hL/k_0 A_0$  is Biot number, where  $h$  is the thermal conductance of the inter-fiber contact; The interface thermal contact resistance was calculated to be  $6.5 \times 10^{-8} \text{ K}\cdot\text{m}^2\cdot\text{W}^{-1}$  when the graphene sheets are in octane and  $7.7 \times 10^{-8} \text{ K}\cdot\text{m}^2\cdot\text{W}^{-1}$  when the graphene sheets are in vacuum [113].  $\langle N_c \rangle$  is the average contact number among the nanofibers, whose value was derived as  $\langle N_c \rangle = 4rV_f / (2 + \pi V_f)$  for 3D random network;  $n_s$  is the areal number density, whose value was derived as  $n_s = V_f / (2A_0)$  for 3D random networks;  $\langle H \rangle$  is the average center to center distance, whose value was derived as  $\langle H \rangle = 0.1852L$ . In this model,  $B_i$  represents the ratio of intrinsic thermal resistance of the nanofiber and inter-fiber contact resistance. Figure 10 shows the effective  $k$  normalized to the  $k$  of the nanofiber,  $k_e/k_0$  in the random nanofiber networks as a function of  $B_i$  number for different volume fraction. For very small  $B_i$  number range,  $k_e$  decreased following a power law with the change of the thermal resistance of inter-fiber contacts. However, for very large  $B_i$  number,  $k_e$  reached a constant, indicating that the effect of inter-fiber contact resistance becomes insignificant compared to the thermal resistance of the nanofibers.

However, neither the rule of mixtures, the EMT approximations, or Zhao's model take the details of the microstructure of the GAs (pore size, shape, or the closed pores, etc.) into consideration. Due to the existence of closed pores,  $k$  of the air in the pores is greatly suppressed. In this case,  $k$  of the air differs greatly from that of

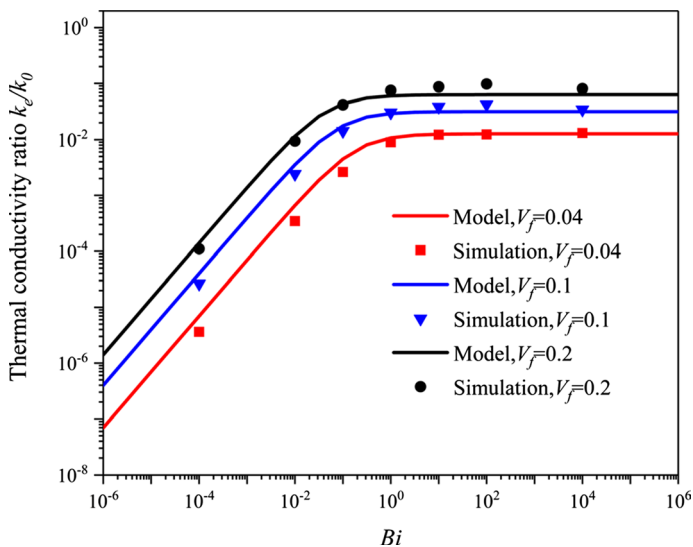


**Fig. 10** The effective  $k$  normalized to  $k$  of the nanofiber,  $k_e/k_0$ , in the random nanofiber networks as a function of  $Bi$  according to Eq. 14 and numerical simulations, respectively. The input parameters are  $r = 500$  and  $D = 3 \text{ nm}$  [115]. (Reproduced from Ref. [115], with the permission of AIP Publishing)

free air. Therefore, in order to further clarify the synergistic effect of solid and pore structure on the effective thermal conductivity, further study is required to establish a gas–solid coupled heat transfer model for the specific self-assembled microstructure of GAs.

### 5.2 The Intrinsic $\alpha$ and $k$ of Graphene Nano-flakes

The  $k$  of GAs is significantly influenced by two factors. One factor is the assembling pattern (pore size and morphology, porosity, etc.), and the other factor is the intrinsic  $k$  of the nano-flakes within GAs. The intrinsic  $k$  and  $\alpha$  refer to the  $k$  and  $\alpha$  of the solid constituents in GAs. By taking the micro-structure into consideration, the intrinsic  $k$  and  $\alpha$  of the graphene nanoflakes can be determined. Pettes et al. used the model of Schuetz et al. for calculating  $k$  of the few-layered graphene in the open-celled GF materials [105]. From the Schuetz and Glicksman model, the intrinsic  $\alpha$  of the solid for porous media can be estimated as: [105, 116]

$$k_G = 3k_{GA}/\varphi \tag{15}$$

In this equation,  $k_{GA}$  is the effective  $k$  of GA,  $\varphi = \rho_{GA}/\rho_G$  is the volume fraction of solid r-GO framework in GAs.  $\rho_{GA}$  of the samples can be determined by measuring the mass and the volume of the samples and  $\rho_G$  can be assumed equal to that of graphite in the literature [93] ( $\rho_G = 2230 \text{ mg}\cdot\text{cm}^{-3}$ ).

However, in Pettes et al.’s work, an uncertainty of about 10–20% existed in their results, which was mainly due to the uncertainty from measuring  $\varphi$ . To avoid the

error from measuring  $\varphi$ , Lin et al. further developed this model in the form of  $\alpha$  [94]. Based on Eq. 15, dividing both sides of equation by the  $c_p$  of graphene transforms Eq. 15 to be:

$$\alpha_G = 3\alpha_{GF} \quad (16)$$

where  $\alpha_G$  and  $\alpha_{GF}$  are the solid  $\alpha$  of the graphene nano-flakes and the effective  $\alpha$  of GF, respectively. By using this model, without knowing the volume fraction (porosity) of the GF sample, the intrinsic  $\alpha$  of graphene can be directly determined from the effective  $\alpha$  of the GF sample.

On the other hand, considering that the graphene nano-sheets inside GA are randomly oriented, the suspended length  $L$  is not the length of the actual heat transfer path of phonons inside the GA. In fact, the actual heat transfer path is a curved route instead of a straight line. The actual heat transfer route can also be evaluated for studying the intrinsic  $k$  and  $\alpha$  of the graphene nanoflakes. Xie et al. evaluated the actual route of heat transfer in CNT bundles [93]. As plotted in the Fig. 11a, the CNT bundles were arranged along the axial direction, while the single CNT bundles were not straight from the SEM image as shown in Fig. 11b. Thus, the heat transfer path between points A and B should be along the curved red line, instead of along the straight route between them (blue line). Therefore, the actual heat transfer paths were much longer than the length of CNT bundle sample. The 3D ratio of the curvature length of CNTs over the straight line length was estimated as 1.52. For one-dimensional heat transfer model, the normalized temperature profile during TET measurement is derived as that in Eq. 7. Based on Eq. 7,  $\alpha$  is proportional to  $L^2$ . Thus, the corresponding ratio of  $\alpha_{intrinsic}$  to  $\alpha_{effective}$  was determined to be 2.31 for the CNT bundles. Lin et al. also used this method for estimating the intrinsic  $\alpha$  of graphene flakes inside GF. The ratios of actual heat transfer route versus the straight line distance was determined as  $\sqrt{L_x^2 + L_y^2 + L_z^2} = 1.90$  and 1.46 for GF samples 1

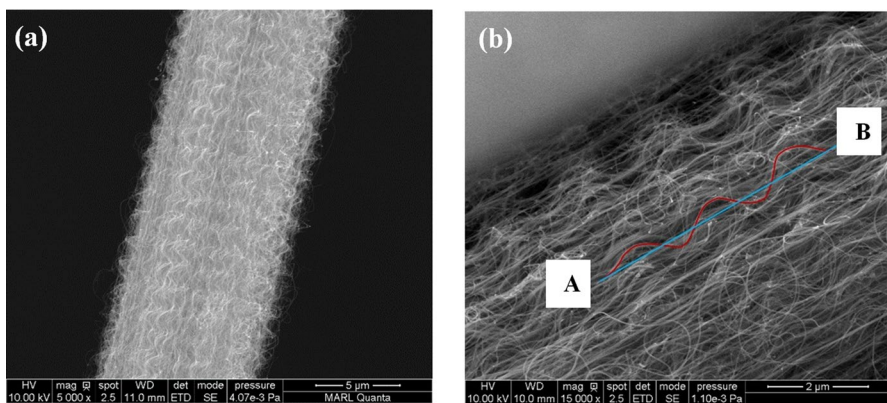


**Fig. 11** Morphology and structure characterization of CNT bundles. (a), (b) SEM images of the CNT bundles under  $\times 500$  and  $\times 15\,000$  magnifications. The heat transfer path between points A and B should be along the curved red line, instead of along the straight route between them (blue line) [93]. (Reproduced from Ref. [93], with the permission from Elsevier)

and 2, respectively [94]. Thus, the corresponding ratio of  $\alpha_G$  to  $\alpha_{GF}$  was determined to be 3.61 and 2.14 for the two GF samples, respectively, which agreed well with the factor of 3 used in the Schuetz's model in Eq. 16.

### 5.3 Effect of Structural Defects

For the intrinsic  $k$  and  $\alpha$  of the graphene nanoflakes, structure defects play an important role. Defects including charged impurities [117], functionalized groups [118], Stone–Wales defects, vacancy defects, stains, etc. are very complex, which are responsible for the large discrepancy existed among the experimental results of  $k$  of graphene. To quantify the relation between structural defects and thermal properties, the thermal reffusivity ( $\Theta$ ) model has been developed in recent years for directly characterizing the underlying phonons scattering mechanisms [119]. From the  $\Theta$  against temperature curves, the phonon scattering behavior, structure defects and domain size of materials can be uncovered. In addition, the Debye temperature of the material and the ideal  $\alpha$  of single perfect crystals can also be evaluated.

According to Wiedemann–Franz law, the contribution of electrons only takes a small portion about 0.2 % to 3.6 % of effective  $k$  of graphene [105], which is negligible. Thus, phonons are the main heat carriers in GA. The phonon propagation in GA is affected by several phonon scattering mechanisms, which includes the scattering from other phonons and that from lattice defects, chemical impurities, grain boundaries, and rough edges, etc. [93]. To characterize the phonon scattering mechanisms,  $\Theta$  of phonons was defined first by Xu et al. as:

$$\Theta = 1/\alpha. \quad (17)$$

Based on the Matthiessen Rule, the total phonon scattering intensity can be obtained by the linear superposition of all the scattering effects. Therefore, the total phonon scattering intensity can be derived as [103]:

$$\frac{1}{\tau} = \frac{1}{\tau_d} + \frac{1}{\tau_p} \quad (18)$$

In this equation,  $\tau_d$  and  $\tau_p$  are the phonon relaxation time from the defects induced phonon scattering and phonon to phonon scattering, respectively. The phonon relaxation time  $\tau$  is inversely proportional to the phonon scattering intensity.  $\tau_p$  is related to the lattice vibration, which is weakened as the temperature goes down [3, 103]. When the temperature approaches to near 0 K, the population of phonons involved in the phonon–phonon scattering significantly reduces, which makes the  $(\tau_p)^{-1}$  term reaches zero. On the other hand, for normal materials with continuous structure, the defect can be regarded an inherent property of the material [96]. Thus,  $\tau_d$  can be assumed to be a constant and independent of temperature for normal materials with continuous structure. In this way, when the temperature is lowered down to near 0 K, the equation of the total phonon scattering intensity reduced to:  $(\tau)^{-1} = (\tau_d)^{-1}$ .

From kinetic theory of gases [19],  $k$  of graphene based materials can be expressed as  $k = Cvl_s/3$ , where  $C$  is the energy carriers'  $c_p$  per unit volume,  $v$  is the average particle velocity, and  $l_s$  is the mean free path of the particles between



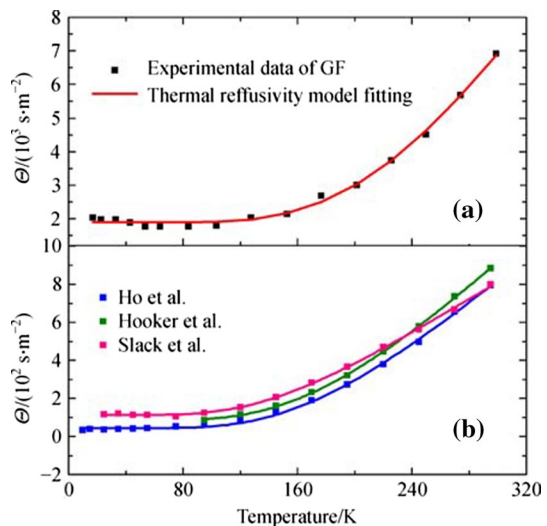
two consecutive collisions. By dividing both sides of equation by  $c_p$ , the relationship of the  $\Theta$  and the phonon scattering intensity can be expressed as  $\alpha = v^2\tau/3$ , which makes  $\Theta = 1/\alpha = 3/v^2\tau$  [96]. Therefore, the thermal reffusivity model has been deduced as:

$$\Theta = \frac{3}{v^2} \left( \frac{1}{\tau_d} + \frac{1}{\tau_p} \right) = \Theta_0 + C \cdot e^{-T_D/2T} \tag{19}$$

In this equation,  $T_D$  is the Debye temperature of the materials,  $C$  is a constant, and  $\Theta_0$  is the residual  $\Theta$  of material [103], which can be obtained by fitting  $\Theta$  to the point of  $T=0$  K. The value of  $\Theta_0$  quantitatively reflects the effect of structural defects scattering inside the material. The value of  $\Theta_0$  of defect-free materials was found to be close to zero [29].

Figure 12a, b present the calculated  $\Theta$  against temperature for GF and three pyrolytic graphite materials, respectively [103]. Obviously, these four fitting curves showed a similar trend: as the temperature decreased from 299 K to 0 K.  $\Theta$  first decreased rapidly and then gradually became stable at temperatures below 100 K, corresponding to their  $\Theta_0$ . As a result, the  $\Theta_0$  were determined to be  $1878 \text{ s}\cdot\text{m}^{-2}$ ,  $43.3 \text{ s}\cdot\text{m}^{-2}$ ,  $84.7 \text{ s}\cdot\text{m}^{-2}$  and  $112.1 \text{ s}\cdot\text{m}^{-2}$  for GF and three pyrolytic graphite materials, respectively. This uncovered a 16–43-fold higher defect level in GF than that in pyrolytic graphite. The Debye temperature of graphene was determined to be 1813 K from the  $\Theta$ -T curve fitting, which was very close to the average theoretical Debye temperature (1911 K) of the three acoustic phonon modes in graphene. By subtracting the defect effect, the ideal  $\alpha$  and  $k$  of graphene nano-flakes in the 3D GF was also reported in Xie et al’s work.

**Fig. 12** The calculated  $\Theta$  of (a) GF and (b) three pyrolytic graphite materials by Xie et al. (Reproduced from Ref. [103], with the permission of RSC Publishing)



## 5.4 Effect of Thermal Contact Resistance

As mentioned above,  $\Theta$  of normal carbon materials with continuous structures show a decreasing trend as the temperature goes down, which reflects the effect of temperature-dependent phonon–phonon scattering. However,  $\Theta$  of weakly interconnected GA could show different behaviors from that of the normal carbon materials. Xie et al. studied the temperature dependent  $\Theta$  of chemically derived GAs [119]. As shown in Fig. 13a,  $\Theta$  of chemically derived GA clearly had an increasing behavior with the decreasing temperature [119], which suggested that the thermal transfer mechanism of GA is completely different from that of the normal carbon-based materials. From the structure point of view, the self-assembled 3D interconnected isotropic network of GA was made up of r-GO nano-sheets. In this way, the thermal contact resistance between two neighboring r-GO sheets was expected to be very large. Based on this fact, a model for heat transfer in GA has been derived by Xie et al. as: [19]

$$l_f/k_{eff} = l_f/k_C + R \quad (20)$$

where  $l_f$  is the average flake size,  $k_{eff}$  is the effective  $k$  of GA, and  $k_C$  is the  $k$  of r-GO sheets.  $R$  is the interfacial thermal contact resistance between two neighboring r-GO sheets. When the  $R$  at interface is very large:  $R \gg l_f/k_C$ , the equation can be transformed to be  $\alpha_{eff} = Avl_f$ , in which  $A$  is a constant, and the phonon velocity  $v$  and  $l_f$  is not dependent on temperature. As a result,  $\Theta$  of GAs can be assumed to be independent of temperature. Thus, the key factor that controlled the thermal transport mechanism in GAs was found to be the thermal contact resistance at interfaces among the r-GO sheets.

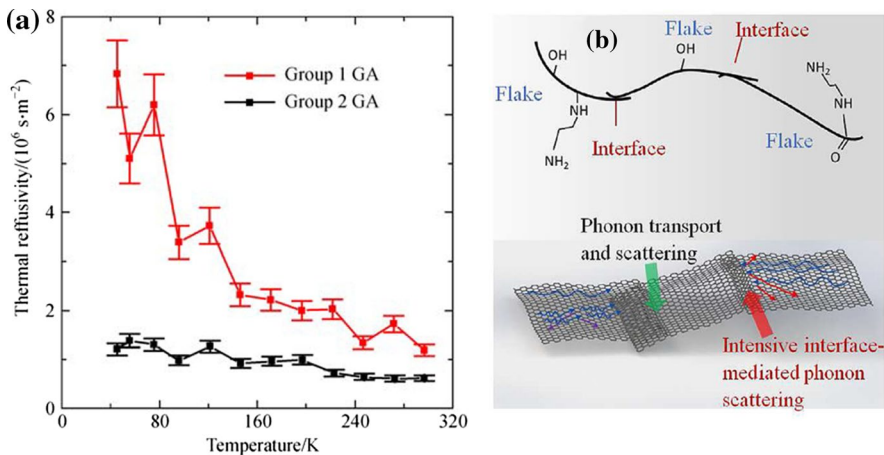


**Fig. 13** (a) The profiles of  $\Theta$  against temperature of two GA samples [119]. (Reproduced from Ref. [119], with the permission of Springer Nature.) (b) The schematic diagram of inter-connection between two neighboring r-GO sheets and the phonon scattering mechanisms [19]. (Reproduced from Ref. [19], with the permission from Elsevier)

Figure 13b is the schematic diagram showing the connection between two neighboring r-GO nano-sheets [19]. The r-GO sheets are combined by  $\pi - \pi$  bonds, which were weak electrostatic attraction between atoms. As the temperature decrease, the interface contact between contiguous r-GO sheets became worse due to thermal expansion of the r-GO sheets, which led to stronger phonon scattering intensity and shorter phonon relaxation time. All of factors contributed to the reduced  $\alpha$  and increasing  $\Theta$  with the lowering temperature. Zhang et al. also found a contrasting behavior of oxidized graphene scaffolds and reduced graphene scaffolds, which was resulted from the large differences in the intersheet contact resistance and varying intrinsic  $k$  between the reduced and oxidized graphene nano-sheets [12]. Therefore, for weakly interconnected GAs, the interface thermal contact resistance among nanoflakes could play a dominating role affecting the overall thermal transport of GAs.

## 6 Concluding Remarks and Outlook

Scaling-up of two-dimensional graphene towards industrial applications is one of the ultimate goals of graphene materials research. Graphene aerogel (GA) as one of the most promising candidates has attracted wide research attentions. Understanding the underlying energy transport mechanisms is essential to the implementation of these 3D structures into energy-based applications, thermal design of sensors, or electronic devices. In this work, we systematically reviewed the synthesis, micro-structure control, thermal characterization, and thermal transport models of GAs.

### 6.1 Challenges Confronted in Current Micro-structure Manipulation Techniques

In order to meet the specific requirements of the novel applications, different micro-structures are often desired. Chemical doping, density and pore structure adjustment, and heterostructure design are widely used in the structure engineering of GAs, which could modify the heat transfer mechanisms inside GAs, leading to different thermal performances. With the deepening of research on graphene materials in recent years, the controllable synthesizing technologies of GAs has been developed rapidly. Among them, the freeze-casting and self-assembly method are the most accessible ones. By controlling the process of replacing the liquid inside hydrogel with gas, different pore structures can be achieved. To reduce the pore size, increasing the freezing rate, decreasing the freezing temperature, or super-critical drying can be used. Meanwhile, extra templates such as polymer spheres, metal wires, or gas bubbles can also be added to introduce the second-level pores. However, achieving GAs with ultra-small pore size (in the range of dozens to hundreds of nanometers) and good mechanical robustness is still challenging. The synthesis requires either expensive supercritical drying facilities or complex chemical procedures. Large scale production of GAs with small pore size, good thermal insulation properties, and strong mechanical elasticity are still in great demand for the future applications.

For the pore morphology design, by controlling the freezing directions, anisotropic pores can be obtained. Further studies are required for finer control so that the size and direction distribution parameters of the pores can well meet the design targets. Besides the experimental approaches, simulations can be conducted in predicting the ice crystals formation process under different temperature gradient scenarios so as to provide theoretical guidance for optimizing the synthesizing procedures. For the heterostructure design, chemical doping brings in more scattering sites for phonons, which is expected to significantly affect the thermal properties of solid matrix in GAs. Additionally, the band gap of the graphene nanoflakes is expected to be changed by the chemical modification or heterostructures, which could improve or alleviate the electron–phonon coupling and brings in new opportunities for the applications of GAs in sensors and electronic devices. Simultaneous and fine control of the density and type of chemical doping of GAs requires further investigation considering the self-assembly process of GAs is very complex. Also the successful introduction of other 1D or 2D heterostructures into GA with good structural control of the density and morphology remains challenging.

## 6.2 Efficient Thermal Characterization

To study the relationship between the microstructures and the thermal performances, experimentally characterizing the thermal properties of these 3D porous materials is essential. For reliable thermal properties results, the effect of thermal radiation and air conduction should be carefully taken into consideration. Although the hot disk method has been used for characterization of the apparent  $k$  of GAs, it does not consider the strong effect of thermal radiation. More importantly, the large thermal contact resistance between the porous sample and the probe brings in significant measurement uncertainty. Thus, the measurement error of apparent  $k$  of GAs by using hot disk method is very high. To avoid the measurement errors from the contact thermal resistance, the non-contact thermal characterization methods based on infrared imaging have been developed. Infrared microscopy technique as a non-contact thermal characterization method has been used for measuring the apparent  $k$  of the bulk GA materials. However, it still requires an accurate temperature scanning of the highly porous GA surface. Likewise, laser flash technique has also been used to measure the apparent  $\alpha$  of carbon foams at room temperature. However, considering the highly rough and porous surface of GA, there is also a certain error in directly using infrared scanning method to measure the temperature distribution of the surface of GA. Therefore, the DLI technique has been further developed to adapt to the unique structure of GA, where only the upper surface temperature of glass wafers needs to be acquired by using the infrared camera. This provides a more accurate method for characterizing the apparent  $k$  of GAs.

Thermal characterization of the solid matrix in GA is also important for both its applications and understanding of its thermal conduction mechanisms. The air conduction effect becomes negligible under vacuum environments. When the pore size is smaller or comparable to the mean free path ( $\lambda$ ) of air molecules ( $\sim 70$  nm), the heat conduction of air within GA is sufficiently suppressed according to the

Knudsen effect. Under this circumstance, the solid heat conduction of the graphene matrix also plays a dominating role in the thermal transport of GA. Two-dimensional graphene nano-sheets are the basic unit of solids that constitute the three-dimensional GA, which are electrically conductive. Therefore, the self-heating and self-sensing electrothermal technologies are applicable for thermal characterization of solid matrix. Compared with other technologies (thermal plane source method,  $3\omega$  method, micro bridge method, [101] etc.) which require either contact, metal coating, or direct infrared scanning, the self-heating and self-sensing electrothermal technologies have the following advantages in measuring the thermal properties of GAs: easy to operate, fast, no additional coating treatment required; low requirements on the surface temperature scanning. The development of the self-heating and self-sensing electrothermal technologies including TET and SET has paved the way for more in-depth study of the thermal properties and heat conduction mechanisms of three-dimensional GA with complex micro-structure design in the future.

### 6.3 Opportunities in Thermal Transport Physical Models

The heat transfer inside GAs is mainly from the coupling of the solid heat transfer, air heat transfer, and radiant heat transfer. The coupling relationship between solid and air thermal conduction and their contribution to effective  $k$  are related to the solid  $k$ , porosity, interconnections, pore size and morphology. For the air–solid coupling models, neither the rule of mixtures, the EMT approximations, or Zhao's model take the details of the microstructure of the GAs (pore size, shape, or the closed pores, etc.) into consideration. Due to the existence of closed pores, when the pore size is smaller or comparable to the mean free path ( $\Lambda$ ) of air molecules ( $\sim 70$  nm),  $k$  of the air in the pores is greatly suppressed. In this case,  $k$  of the air differs greatly from that of free air. The anisotropic pore structure also brings in different thermal conduction behaviors in different directions of GA. Therefore, in order to further clarify the synergistic effect of solid and pore structure on the effective thermal conductivity, further study is required to establish an air–solid coupled heat transfer model for the specific self-assembled microstructure of GAs.

The  $k$  of GAs is significantly influenced by two factors. One factor is the assembling pattern (pore size and morphology, porosity, etc.), and the other factor is the intrinsic  $k$  of the nano-flakes within GAs. Combined with the thermal characterization of solid matrix, the models for the intrinsic thermal diffusivity/conductivity of GA from the heat transfer path method provides a more detailed analysis for the intrinsic thermal properties of the nanoflakes within GA. Structural defects provide a large number of scattering opportunities for the transmission of phonons, thereby inhibiting the thermal conduction. The thermal reffusivity model for analyzing the effect of structure defects on phonon scattering provides some of the best physical model to analyze such structure effects. Due to the unique self-assembling structure of GA, the thermal contact resistance could play a dominant role in the thermal transport of GAs. The interface-mediated thermal conduction model could be used to provide in-depth analysis of the interface effect on heat conduction in GAs. For GAs of different microstructures, the temperature-dependent thermal reffusivity

can be obtained for providing significant information and a clear physical picture about the levels of defects density and interconnection strength within GAs, which is indispensable for a good understanding of the effect of microstructures design on the thermal transport of GA.

**Acknowledgment** Support of this work by National Natural Science Foundation of China (No. 51906161) is gratefully acknowledged.

## Compliance with Ethical Standards

**Conflict of Interest** The authors declare no conflict of interest.

## References

1. C.H. Tan, J. Cao, A.M. Khattak, F.P. Cai, B. Jiang, G. Yang, S.Q. Hu, High-performance tin oxide-nitrogen doped graphene aerogel hybrids as anode materials for lithium-ion batteries. *J. Power Sources* **270**, 28–33 (2014)
2. Q.Q. Ke, J. Wang, Graphene-based materials for supercapacitor electrodes—a review. *J. Materiomics* **2**(1), 37–54 (2016)
3. Y.S. Xie, M. Han, R.D. Wang, H. Zobeiri, X. Deng, P.X. Zhang, X.W. Wang, Graphene aerogel based bolometer for ultrasensitive sensing from ultraviolet to far-infrared. *ACS Nano* **13**(5), 5385–5396 (2019)
4. M.A. Worsley, P.J. Pauzaukie, T.Y. Olson, J. Biener, J.H. Satcher, T.F. Baumann, Synthesis of graphene aerogel with high electrical conductivity. *J. Am. Chem. Soc.* **132**(40), 14067–14069 (2010)
5. X.T. Zhang, Z.Y. Sui, B. Xu, S.F. Yue, Y.J. Luo, W.C. Zhan, B. Liu, Mechanically strong and highly conductive graphene aerogel and its use as electrodes for electrochemical power sources. *J. Mater. Chem.* **21**(18), 6494–6497 (2011)
6. Z.Y. Sui, Q.H. Meng, X.T. Zhang, R. Ma, B. Cao, Green synthesis of carbon nanotube-graphene hybrid aerogels and their use as versatile agents for water purification. *J. Mater. Chem.* **22**(18), 8767–8771 (2012)
7. J. Li, F. Wang, C.Y. Liu, Tri-isocyanate reinforced graphene aerogel and its use for crude oil adsorption. *J. Colloid Interface Sci.* **382**, 13–16 (2012)
8. J.H. Li, J.Y. Li, H. Meng, S.Y. Xie, B.W. Zhang, L.F. Li, H.J. Ma, J.Y. Zhang, M. Yu, Ultra-light, compressible and fire-resistant graphene aerogel as a highly efficient and recyclable absorbent for organic liquids. *J. Mater. Chem. A* **2**(9), 2934–2941 (2014)
9. X. Li, T. Liu, D. Wang, Q. Li, Z. Liu, N. Li, Y. Zhang, C. Xiao, X. Feng, Superlight adsorbent sponges based on graphene oxide cross-linked with poly(vinyl alcohol) for continuous flow adsorption. *ACS Appl. Mater. Interfaces.* **10**(25), 21672–21680 (2018)
10. Z.S. Wu, Y. Sun, Y.Z. Tan, S.B. Yang, X.L. Feng, K. Mullen, Three-dimensional graphene-based macro- and mesoporous frameworks for high-performance electrochemical capacitive energy storage. *J. Am. Chem. Soc.* **134**(48), 19532–19535 (2012)
11. Q.Q. Zhang, X. Xu, H. Li, G.P. Xiong, H. Hu, T.S. Fisher, Mechanically robust honeycomb graphene aerogel multifunctional polymer composites. *Carbon* **93**, 659–670 (2015)
12. Q.Q. Zhang, M.L. Hao, X. Xu, G.P. Xiong, H. Li, T.S. Fisher, Flyweight 3D graphene scaffolds with microinterface barrier-derived tunable thermal insulation and flame retardancy. *ACS Appl. Mater. Interfaces.* **9**(16), 14232–14241 (2017)
13. D.P. Dong, H.T. Guo, G.Y. Li, L.F. Yan, X.T. Zhang, W.H. Song, Assembling hollow carbon sphere-graphene polyolithic aerogels for thermoelectric cells. *Nano Energy* **39**, 470–477 (2017)
14. Y. Fu, G. Wang, X. Ming, X.H. Liu, B.F. Hou, T. Mei, J.H. Li, J.Y. Wang, X.B. Wang, Oxygen plasma treated graphene aerogel as a solar absorber for rapid and efficient solar steam generation. *Carbon* **130**, 250–256 (2018)
15. Y.F. Liu, Q.W. Shi, C.Y. Hou, Q.H. Zhang, Y.G. Li, H.Z. Wang, Versatile mechanically strong and highly conductive chemically converted graphene aerogels. *Carbon* **125**, 352–359 (2017)

16. Y.J. Zhong, M. Zhou, F.Q. Huang, T.Q. Lin, D.Y. Wan, Effect of graphene aerogel on thermal behavior of phase change materials for thermal management. *Sol. Energy Mater. Sol. Cells* **113**, 195–200 (2013)
17. J. Yang, E.W. Zhang, X.F. Li, Y.T. Zhang, J. Qu, Z.Z. Yu, Cellulose/graphene aerogel supported phase change composites with high thermal conductivity and good shape stability for thermal energy storage. *Carbon* **98**, 50–57 (2016)
18. C.W. Yue, J. Feng, J.Z. Feng, Y.G. Jiang, Low-thermal-conductivity nitrogen-doped graphene aerogels for thermal insulation. *Rsc Adv.* **6**(12), 9396–9401 (2016)
19. Y.S. Xie, S. Xu, Z.L. Xu, H.C. Wu, C. Deng, X.W. Wang, Interface-mediated extremely low thermal conductivity of graphene aerogel. *Carbon* **98**, 381–390 (2016)
20. P.A. George, J. Strait, J. Dawlaty, S. Shivaraman, M. Chandrashekhara, F. Rana, M.G. Spencer, Ultrafast optical-pump terahertz-probe spectroscopy of the carrier relaxation and recombination dynamics in epitaxial graphene. *Nano Lett.* **8**(12), 4248–4251 (2008)
21. T.T. Miao, S.Y. Shi, S. Yan, W.G. Ma, X. Zhang, K. Takahashi, T. Ikuta, Integrative characterization of the thermoelectric performance of an individual multiwalled carbon nanotube. *J. Appl. Phys.* **120**(12), 6 (2016)
22. Y.F. Zhang, A.R. Fan, S.T. Luo, H.D. Wang, W.G. Ma, X. Zhang, Suspended 2D anisotropic materials thermal diffusivity measurements using dual-wavelength flash Raman mapping method. *Int. J. Heat Mass Transfer* **145**, 1 (2019)
23. P. Kim, L. Shi, A. Majumdar, P.L. McEuen, Thermal transport measurements of individual multiwalled nanotubes. *Phys. Rev. Lett.* **87**, 21 (2001)
24. T.Y. Choi, D. Poulikakos, J. Tharian, U. Sennhauser, Measurement of thermal conductivity of individual multiwalled carbon nanotubes by the 3-omega method. *Appl. Phys. Lett.* **87**, 1 (2005)
25. T. Baba, A. Ono, Improvement of the laser flash method to reduce uncertainty in thermal diffusivity measurements. *Meas. Sci. Technol.* **12**(12), 2046–2057 (2001)
26. X.W. Wang, Z.R. Zhong, J. Xu, Noncontact thermal characterization of multiwall carbon nanotubes. *J. Appl. Phys.* **97**, 6 (2005)
27. J.Y. Hong, J.J. Wie, Y. Xu, H.S. Park, Chemical modification of graphene aerogels for electrochemical capacitor applications. *Phys. Chem. Chem. Phys.* **17**(46), 30946–30962 (2015)
28. L.S. Chen, X.Z. Cui, Y.X. Wang, M. Wang, R.H. Qiu, Z. Shu, L.X. Zhang, Z.L. Hua, F.M. Cui, C.Y. Weia, J.L. Shi, One-step synthesis of sulfur doped graphene foam for oxygen reduction reactions. *Dalton Trans.* **43**(9), 3420–3423 (2014)
29. Z. Fan, A. Marconnet, S.T. Nguyen, C.Y.H. Lim, H.M. Duong, Effects of heat treatment on the thermal properties of highly nanoporous graphene aerogels using the infrared microscopy technique. *Int. J. Heat Mass Transf.* **76**, 122–127 (2014)
30. Q.Y. Peng, Y.Y. Qin, X. Zhao, X.X. Sun, Q. Chen, F. Xu, Z.S. Lin, Y. Yuan, Y. Li, J.J. Li, W.L. Yin, C. Gao, F. Zhang, X.D. He, Y.B. Li, Superlight, mechanically flexible, thermally superinsulating, and antifrosting anisotropic nanocomposite foam based on hierarchical graphene oxide assembly. *ACS Appl. Mater. Interfaces* **9**(50), 44010–44017 (2017)
31. E. Garcia-Bordeje, S. Victor-Roman, O. Sanahuja-Parejo, A.M. Benito, W.K. Maser, Control of the microstructure and surface chemistry of graphene aerogels via pH and time manipulation by a hydrothermal method. *Nanoscale* **10**(7), 3526–3539 (2018)
32. D. Tomanek, S. Berber, K. Umemoto, S. Saito, Hierarchical assembly of nanostructured carbon foam. *Mol. Cryst. Liq. Cryst.* **386**, 189–195 (2002)
33. C.H. Wang, X. Chen, B. Wang, M. Huang, B. Wang, Y. Jiang, R.S. Ruoff, Freeze-casting produces a graphene oxide aerogel with a radial and centrosymmetric structure. *ACS Nano* **12**(6), 5816–5825 (2018)
34. W.Z. Xu, Y. Xing, J. Liu, H.P. Wu, Y. Cuo, D.W. Li, D.Y. Guo, C.R. Li, A.P. Liu, H. Bai, Efficient water transport and solar steam generation via radially, hierarchically structured aerogels. *Acs Nano* **13**(7), 7930–7938 (2019)
35. M. Yang, N.F. Zhao, Y. Cui, W.W. Gao, Q. Zhao, C. Gao, H. Bai, T. Xie, Biomimetic architected graphene aerogel with exceptional strength and resilience. *ACS Nano* **11**(7), 6817–6824 (2017)
36. Y.X. Xu, K.X. Sheng, C. Li, G.Q. Shi, Self-assembled graphene hydrogel via a one-step hydrothermal process. *ACS Nano* **4**(7), 4324–4330 (2010)
37. W.F. Chen, L.F. Yan, In situ self-assembly of mild chemical reduction graphene for three-dimensional architectures. *Nanoscale* **3**(8), 3132–3137 (2011)

38. B. Yao, S. Chandrasekaran, H.Z. Zhang, A. Ma, J.Z. Kang, L. Zhang, X.H. Lu, F. Qian, C. Zhu, E.B. Duoss, C.M. Spadaccini, M.A. Worsley, Y. Li, 3D-Printed structure boosts the kinetics and intrinsic capacitance of pseudocapacitive graphene aerogels. *Adv. Mater.* **32**, 8 (2020)
39. X.J. Xu, P.Y. Li, L. Zhang, X.J. Liu, H.L. Zhang, Q.Z. Shi, B.J. He, W.J. Zhang, Z. Qu, P. Liu, Covalent functionalization of graphene by nucleophilic addition reaction: synthesis and optical-limiting properties. *Chem. Asian J.* **12**(19), 2583–2590 (2017)
40. E. Garcia-Tunon, S. Barg, J. Franco, R. Bell, S. Eslava, E. D'Elia, R.C. Maher, F. Guitian, E. Saiz, Printing in three dimensions with graphene. *Adv. Mater.* **27**(10), 1688–1693 (2015)
41. C. Zhu, T.Y.J. Han, E.B. Duoss, A.M. Golobic, J.D. Kuntz, C.M. Spadaccini, M.A. Worsley, Highly compressible 3D periodic graphene aerogel microlattices. *Nat. Commun.* **6**, 23 (2015)
42. Y.X. Xu, W.J. Hong, H. Bai, C. Li, G.Q. Shi, Strong and ductile poly(vinyl alcohol)/graphene oxide composite films with a layered structure. *Carbon* **47**(15), 3538–3543 (2009)
43. E. Greco, J. Shang, J.L. Zhu, T. Zhu, Synthesis of polyacetylene-like modified graphene oxide aerogel and its enhanced electrical properties. *ACS Omega* **4**(25), 20948–20954 (2019)
44. F. Jiang, H. Liu, Y. Li, Y.D. Kuang, X. Xu, C.J. Chen, H. Huang, C. Jia, X.P. Zhao, E. Hitz, Y.B. Zhou, R.G. Yang, L.F. Cui, L.B. Hu, Lightweight, mesoporous, and highly absorptive all-nanofiber aerogel for efficient solar steam generation. *ACS Appl. Mater. Interfaces* **10**(1), 1104–1112 (2018)
45. B. Wicklein, A. Kocjan, G. Salazar-Alvarez, F. Carosio, G. Camino, M. Antonietti, L. Bergstrom, Thermally insulating and fire-retardant lightweight anisotropic foams based on nanocellulose and graphene oxide. *Nat. Nanotechnol.* **10**(3), 277–283 (2015)
46. P.P. Zhang, J. Li, L.X. Lv, Y. Zhao, L.T. Qu, Vertically aligned graphene sheets membrane for highly efficient solar thermal generation of clean water. *ACS Nano* **11**(5), 5087–5093 (2017)
47. Y.M. Yao, Y.M. Li, X.L. Zeng, N. Sun, R. Sun, J.B. Xu, C.P. Wong, Liquid nitrogen driven assembly of nanomaterials into spongy millispheres for various applications. *J. Mater. Chem. A* **6**(14), 5984–5992 (2018)
48. M.W. Pot, K.A. Faraj, A. Adawy, W.J.P. van Enckevort, H.T.B. van Moerkerk, E. Vlieg, W.F. Daamen, T.H. van Kuppevelt, Versatile wedge-based system for the construction of unidirectional collagen scaffolds by directional freezing: practical and theoretical considerations. *ACS Appl. Mater. Interfaces* **7**(16), 8495–8505 (2015)
49. H. Hu, Z.B. Zhao, W.B. Wan, Y. Gogotsi, J.S. Qiu, Ultralight and highly compressible graphene aerogels. *Adv. Mater.* **25**(15), 2219–2223 (2013)
50. H.C. Bi, K.B. Yin, X. Xie, Y.L. Zhou, N. Wan, F. Xu, F. Banhart, L.T. Sun, R.S. Ruoff, Low temperature casting of graphene with high compressive strength. *Adv. Mater.* **24**(37), 5124–5129 (2012)
51. H.Y. Sun, Z. Xu, C. Gao, Multifunctional, ultra-flyweight, synergistically assembled carbon aerogels. *Adv. Mater.* **25**(18), 2554–2560 (2013)
52. Z.H. Tang, S.L. Shen, J. Zhuang, X. Wang, Noble-metal-promoted three-dimensional macroassembly of single-layered graphene oxide. *Angewandte Chemie-Int. Ed.* **49**(27), 4603–4607 (2010)
53. W.F. Chen, S.R. Li, C.H. Chen, L.F. Yan, Self-assembly and embedding of nanoparticles by in situ reduced graphene for preparation of a 3D graphene/nanoparticle aerogel. *Adv. Mater.* **23**(47), 5679–5683 (2011)
54. S. Nardecchia, D. Carriazo, M.L. Ferrer, M.C. Gutierrez, F. del Monte, Three dimensional macroporous architectures and aerogels built of carbon nanotubes and/or graphene: synthesis and applications. *Chem. Soc. Rev.* **42**(2), 794–830 (2013)
55. P. Wu, B. Zhang, Z. Yu, H.W. Zou, P.B. Liu, Anisotropic polyimide aerogels fabricated by directional freezing. *J. Appl. Polym. Sci.* **136**, 11 (2019)
56. Y.M. Yao, X.D. Zhu, X.L. Zeng, R. Sun, J.B. Xu, C.P. Wong, Vertically aligned and interconnected SiC nanowire networks leading to significantly enhanced thermal conductivity of polymer composites. *ACS Appl. Mater. Interfaces.* **10**(11), 9669–9678 (2018)
57. Y. Cui, H.X. Gong, Y.J. Wang, D.W. Li, H. Bai, A thermally insulating textile inspired by polar bear hair. *Adv. Mater.* **30**, 14 (2018)
58. Z. Fan, D.Z.Y. Tng, C.X.T. Lim, P. Liu, S.T. Nguyen, P.F. Xiao, A. Marconnet, C.Y.H. Lim, H.M. Duong, Thermal and electrical properties of graphene/carbon nanotube aerogels. *Colloids Surf.* **445**, 48–53 (2014)
59. Y. Chen, S. Yang, D.B. Fan, G.Y. Li, S.Q. Wang, Dual-enhanced hydrophobic and mechanical properties of long-range 3D anisotropic binary-composite nanocellulose foams via bidirectional gradient freezing. *ACS Sustain. Chem. Eng.* **7**(15), 12878–12886 (2019)



60. D.C. Wu, F. Xu, B. Sun, R.W. Fu, H.K. He, K. Matyjaszewski, Design and preparation of porous polymers. *Chem. Rev.* **112**(7), 3959–4015 (2012)
61. H.J. Zhan, K.J. Wu, Y.L. Hu, J.W. Liu, H. Li, X. Guo, J. Xu, Y. Yang, Z.L. Yu, H.L. Gao, X.S. Luo, J.F. Chen, Y. Ni, S.H. Yu, Biomimetic carbon tube aerogel enables super-elasticity and thermal insulation. *Chem* **5**(7), 1871–1882 (2019)
62. C. Jimenez-Saelices, B. Seantier, B. Cathala, Y. Grohens, Effect of freeze-drying parameters on the microstructure and thermal insulating properties of nanofibrillated cellulose aerogels. *J. Sol-Gel. Sci. Technol.* **84**(3), 475–485 (2017)
63. M. Yang, J.J. Wu, H. Bai, T. Xie, Q. Zhao, T.W. Wong, Controlling three-dimensional ice template via two-dimensional surface wetting. *AIChE J.* **62**(12), 4186–4192 (2016)
64. Y.P. Cui, W. Liu, X. Wang, J.J. Li, Y. Zhang, Y.X. Du, S. Liu, H.L. Wang, W.T. Feng, M. Chen, Bioinspired mineralization under freezing conditions: an approach to fabricate porous carbons with complicated architecture and superior K<sup>+</sup> storage performance. *ACS Nano* **13**(10), 11582–11592 (2019)
65. H. Bai, Y. Chen, B. Delattre, A.P. Tomsia, R.O. Ritchie, Bioinspired large-scale aligned porous materials assembled with dual temperature gradients. *Sci. Adv.* **1**, 111 (2015)
66. J.K. Han, G.L. Du, W.W. Gao, H. Bai, An anisotropically high thermal conductive boron nitride/epoxy composite based on nacre-mimetic 3D network. *Adv. Funct. Mater.* **29**, 13 (2019)
67. G.F. Shao, D.A.H. Hanaor, X.D. Shen, A. Gurlu, Freeze casting: from low-dimensional building blocks to aligned porous structures—a review of novel materials, methods, and applications. *Adv. Mater.* **32**(17), 123 (2020)
68. F. An, X.F. Li, P. Min, H.F. Li, Z. Dai, Z.Z. Yu, Highly anisotropic graphene/boron nitride hybrid aerogels with long-range ordered architecture and moderate density for highly thermally conductive composites. *Carbon* **126**, 119–127 (2018)
69. B. Li, S. Dong, X. Wu, C.P. Wang, X.J. Wang, J. Fang, Anisotropic thermal property of magnetically oriented carbon nanotube/graphene polymer composites. *Compos. Sci. Technol.* **147**, 52–61 (2017)
70. Z.H. Wu, C. Xu, C.Q. Ma, Z.B. Liu, H.M. Cheng, W.C. Ren, Synergistic effect of aligned graphene nanosheets in graphene foam for high-performance thermally conductive composites. *Adv. Mater.* **31**, 19 (2019)
71. B.B. Huo, D.G. Jiang, X.Y. Cao, H. Liang, Z. Liu, C.W. Li, J.Q. Liu, N-doped graphene/carbon hybrid aerogels for efficient solar steam generation. *Carbon* **142**, 13–19 (2019)
72. X. Deng, Q.C. Nie, Y. Wu, H.S. Fang, P.X. Zhang, Y.S. Xie, Nitrogen-doped unusually superwetting, thermally insulating, and elastic graphene aerogel for efficient solar steam generation. *ACS Appl. Mater. Interfaces.* **12**(23), 26200–26212 (2020)
73. J.C. Wang, R.G. Ma, Z.Z. Zhou, G.H. Liu, Q. Liu, Magnesiothermic synthesis of sulfur-doped graphene as an efficient metal-free electrocatalyst for oxygen reduction. *Scientific Reports* **5**, 22 (2015)
74. X.M. Feng, J.L. Zhao, D.W. Sun, L. Shanmugam, J.K. Kim, J.L. Yang, Novel onion-like graphene aerogel beads for efficient solar vapor generation under non-concentrated illumination. *J. Mater. Chem. A* **7**(9), 4400–4407 (2019)
75. H. Long, A. Harley-Trochimczyk, T. Pham, Z.R. Tang, T.L. Shi, A. Zettl, C. Carraro, M.A. Worsley, R. Maboudian, High surface area MoS<sub>2</sub>/graphene hybrid aerogel for ultrasensitive NO<sub>2</sub> detection. *Adv. Funct. Mater.* **26**(28), 5158–5165 (2016)
76. L. Bao, T. Li, S. Chen, C. Peng, L. Li, Q. Xu, Y.S. Chen, E.C. Ou, W.J. Xu, 3D graphene frameworks/Co<sub>3</sub>O<sub>4</sub> Composites electrode for high-performance supercapacitor and enzymeless glucose detection. *Small* **13**, 5 (2017)
77. F. Razmjooei, K.P. Singh, M.Y. Song, J.S. Yu, Enhanced electrocatalytic activity due to additional phosphorous doping in nitrogen and sulfur-doped graphene: a comprehensive study. *Carbon* **78**, 257–267 (2014)
78. Y.H. Xue, D.S. Yu, L.M. Dai, R.G. Wang, D.Q. Li, A. Roy, F. Lu, H. Chen, Y. Liu, J. Qu, Three-dimensional B, N-doped graphene foam as a metal-free catalyst for oxygen reduction reaction. *Phys. Chem. Chem. Phys.* **15**(29), 12220–12226 (2013)
79. T.T. Zhang, J.H. Li, Y.W. Cao, L.Y. Zhu, G.B. Chen, Tailoring thermal transport properties of graphene by nitrogen doping. *J. Nanoparticle Res.* **19**, 2 (2017)
80. I.K. Moon, S. Yoon, K.Y. Chun, J. Oh, Highly elastic and conductive N-doped monolithic graphene aerogels for multifunctional applications. *Adv. Funct. Mater.* **25**(45), 6976–6984 (2015)

81. Y.Z. Su, Y. Zhang, X.D. Zhuang, S. Li, D.Q. Wu, F. Zhang, X.L. Feng, Low-temperature synthesis of nitrogen/sulfur co-doped three-dimensional graphene frameworks as efficient metal-free electrocatalyst for oxygen reduction reaction. *Carbon* **62**, 296–301 (2013)
82. S.B. Yang, L.J. Zhi, K. Tang, X.L. Feng, J. Maier, K. Mullen, Efficient synthesis of heteroatom (N or S)-doped graphene based on ultrathin graphene oxide-porous silica sheets for oxygen reduction reactions. *Adv. Func. Mater.* **22**(17), 3634–3640 (2012)
83. R.T. Lu, C. Christianson, B. Weintrub, J.Z. Wu, High photoresponse in hybrid graphene-carbon nanotube infrared detectors. *ACS Appl. Mater. Interfaces.* **5**(22), 11703–11707 (2013)
84. B.F. Cai, Y.J. Su, Z.J. Tao, J. Hu, C. Zou, Z. Yang, Y.F. Zhang, Highly sensitive broadband single-walled carbon nanotube photodetectors enhanced by separated graphene nanosheets. *Adv. Opt. Mater.* **6**, 23 (2018)
85. X.B. Li, S.W. Yang, J. Sun, P. He, X.G. Xu, G.Q. Ding, Tungsten oxide nanowire-reduced graphene oxide aerogel for high-efficiency visible light photocatalysis. *Carbon* **78**, 38–48 (2014)
86. J. Wang, J.L. Liu, J.S. Luo, P. Liang, D.L. Chao, L.F. Lai, J.Y. Lin, Z.X. Shen, MoS<sub>2</sub> architectures supported on graphene foam/carbon nanotube hybrid films: highly integrated frameworks with ideal contact for superior lithium storage. *J. Mater. Chem. A* **3**(34), 17534–17543 (2015)
87. J. Wang, J.L. Liu, D.L. Chao, J.X. Yan, J.Y. Lin, Z.X. Shen, Self-assembly of honeycomb-like MoS<sub>2</sub> nanoarchitectures anchored into graphene foam for enhanced lithium-ion storage. *Adv. Mater.* **26**(42), 7162–7169 (2014)
88. Q. Wang, J. Dai, X. He, Influence factors analysis of thermal conductivity measurement with hot disk technique. *J. Tianjin Univ.* **2**, 970–974 (2009)
89. H. Zhang, Y. Jin, W. Gu, Z.Y. Li, W.Q. Tao, A numerical study on the influence of insulating layer of the hot disk sensor on the thermal conductivity measuring accuracy. *Prog. Comput. Fluid Dyn.* **13**(3–4), 191–201 (2013)
90. Q. Zheng, S. Kaur, C. Dames, R.S. Prasher, Analysis and improvement of the hot disk transient plane source method for low thermal conductivity materials. *Int. J. Heat Mass Transfer* **151**, 198 (2020)
91. H. Ghasemi, G. Ni, A.M. Marconnet, J. Loomis, S. Yerci, N. Miljkovic, G. Chen, Solar steam generation by heat localization. *Nat. Commun.* **5**, 9 (2014)
92. H.G. Liu, T.H. Li, Y.C. Shi, X. Zhao, Thermal insulation composite prepared from carbon foam and silica aerogel under ambient pressure. *J. Mater. Eng. Perform.* **24**(10), 4054–4059 (2015)
93. Y. Xie, T. Wang, B. Zhu, C. Yan, P. Zhang, X. Wang, G. Eres, 19-Fold thermal conductivity increase of carbon nanotube bundles toward high-end thermal design applications. *Carbon* **139**, 445–458 (2018)
94. H. Lin, S. Xu, X. Wang, N. Mei, Significantly reduced thermal diffusivity of free-standing two-layer graphene in graphene foam. *Nanotechnology* **24**, 41 (2013)
95. J. Guo, X. Wang, T. Wang, Thermal characterization of microscale conductive and nonconductive wires using transient electrothermal technique. *J. Appl. Phys.* **101**(6), 2222 (2007)
96. J. Liu, Z. Xu, Z. Cheng, S. Xu, X. Wang, Thermal conductivity of ultrahigh molecular weight polyethylene crystal: defect effect uncovered by 0 K limit phonon diffusion. *ACS Appl. Mater. Interfaces* **7**(49), 27279–27288 (2015)
97. Z.L. Xu, X.W. Wang, H.Q. Xie, Promoted electron transport and sustained phonon transport by DNA down to 10 K. *Polymer* **55**(24), 6373–6380 (2014)
98. C.H. Xing, T. Munro, C. Jensen, B. White, H. Ban, C.G. Copeland, R.V. Lewis, Thermophysical property measurement of electrically nonconductive fibers by the electrothermal technique. *Meas. Sci. Technol.* **25**(11), 89 (2014)
99. S.E. Gustafsson, Transient plane source techniques for thermal conductivity and thermal diffusivity measurements of solid materials. *Rev. Sci. Instrum.* **62**(3), 797–804 (1991)
100. D.G. Cahill, Thermal-conductivity measurement from 30-K to 750-K - the 3-omega method. *Rev. Sci. Instrum.* **61**(2), 802–808 (1990)
101. J. Kim, D.-J. Seo, H. Park, H. Kim, H.-J. Choi, W. Kim, Extension of the T-bridge method for measuring the thermal conductivity of two-dimensional materials. *Rev. Sci. Instrum.* **88**(5), 8 (2017)
102. Z. Xu, S. Xu, X. Tang, X. Wang, Energy transport in crystalline DNA composites. *AIP Adv.* **4**(1), 21 (2014)
103. Y. Xie, Z. Xu, S. Xu, Z. Cheng, N. Hashemi, C. Deng, X. Wang, The defect level and ideal thermal conductivity of graphene uncovered by residual thermal reffusivity at the 0 K limit. *Nanoscale* **7**(22), 10101–10110 (2015)

104. J. Moon, K. Weaver, B. Feng, H. Chae, S. Kumar, J.B. Baek, G.P. Peterson, Note: Thermal conductivity measurement of individual poly(ether ketone)/carbon nanotube fibers using a steady-state dc thermal bridge method. *Rev. Sci. Instrum* **83**, 1 (2012)
105. M.T. Pettes, H. Ji, R.S. Ruoff, L. Shi, Thermal transport in three-dimensional foam architectures of few-layer graphene and ultrathin graphite. *Nano Lett.* **12**(6), 2959–2964 (2012)
106. G. Gorgolis, C. Galiotis, Graphene aerogels: a review. *Materials* **4**, 3 (2017)
107. K. Sakai, Y. Kobayashi, T. Saito, A. Isogai, Partitioned airs at microscale and nanoscale: thermal diffusivity in ultrahigh porosity solids of nanocellulose. *Scientific Rep.* **6**, 88 (2016)
108. C.Y. Zhao, Review on thermal transport in high porosity cellular metal foams with open cells. *Int. J. Heat Mass Transf.* **55**(13–14), 3618–3632 (2012)
109. X.W. Wang, X.F. Xu, S.U.S. Choi, Thermal conductivity of nanoparticle-fluid mixture. *J. Thermophys. Heat Transfer* **13**(4), 474–480 (1999)
110. W.D. Kingery, Thermal conductivity14 Conductivity of multicomponent systems. *J. Am. Ceramic Soc.* **42**(12), 617–627 (1959)
111. M.M. Bernal, M. Tortello, S. Colonna, G. Saracco, A. Fina, Thermally and electrically conductive nanopapers from reduced graphene oxide: effect of nanoflakes thermal annealing on the film structure and properties. *Nanomaterials* **7**(12), 88 (2017)
112. K.M.F. Shahil, A.A. Balandin, Graphene-multilayer graphene nanocomposites as highly efficient thermal interface materials. *Nano Lett.* **12**(2), 861–867 (2012)
113. D. Konatham, D.V. Papavassiliou, A. Striolo, Thermal boundary resistance at the graphene-graphene interface estimated by molecular dynamics simulations. *Chem. Phys. Lett.* **527**, 47–50 (2012)
114. P.U. Jepsen, B.M. Fischer, A. Thoman, H. Helm, J.Y. Suh, R. Lopez, R.F. Haglund, Metal-insulator phase transition in a VO<sub>2</sub> thin film observed with terahertz spectroscopy. *Phys. Rev. B* **74**(20), 3840–3845 (2006)
115. X.P. Zhao, C.L. Huang, Q.K. Liu, I.I. Smalyukh, R.G. Yang, Thermal conductivity model for nanofiber networks. *J. Appl. Phys.* **123**(8), 12 (2018)
116. M.A. Schuetz, L.R. Glicksman, A basic study of heat-transfer through foam insulation. *J. Cell. Plast.* **20**(2), 114–121 (1984)
117. J.H. Chen, C. Jang, S. Adam, M.S. Fuhrer, E.D. Williams, M. Ishigami, Charged-impurity scattering in graphene. *Nat. Phys.* **4**(5), 377–381 (2008)
118. H.C. Schniepp, J.L. Li, M.J. McAllister, H. Sai, M. Herrera-Alonso, D.H. Adamson, R.K. Prud'homme, R. Car, D.A. Saville, I.A. Aksay, Functionalized single graphene sheets derived from splitting graphite oxide. *J. Phys. Chem. B* **110**(17), 8535–8539 (2006)
119. Y.S. Xie, B.W. Zhu, J. Liu, Z.L. Xu, X.W. Wang, Thermal reffusivity: uncovering phonon behavior, structural defects, and domain size. *Front. Energy* **12**(1), 143–157 (2018)

**Publisher's Note** Springer Nature remains neutral with regard to jurisdictional claims in published maps and institutional affiliations.